



Topology optimization of electrode patterns for electroosmotic micromixer

Yongbo Deng^{a,*}, Teng Zhou^b, Zhenyu Liu^c, Yihui Wu^a, Shizhi Qian^d, Jan G. Korvink^{e,*}

^a State Key Laboratory of Applied Optics, Changchun Institute of Optics, Fine Mechanics and Physics (CIOMP), Chinese Academy of Sciences, Changchun 130033, China

^b Mechanical and Electrical Engineering College, Hainan University, Haikou 570228, China

^c Changchun Institute of Optics, Fine Mechanics and Physics (CIOMP), Chinese Academy of Sciences, Changchun 130033, China

^d Department of Mechanical and Aerospace Engineering, Old Dominion University, ECSB 1309, 4700 Elkhorn Ave, Norfolk, VA 23529, USA

^e Institute of Microstructure Technology, Karlsruhe Institute of Technology (KIT), Hermann-von-Helmholtzplatz 1, 76344 Eggenstein-Leopoldshafen, Germany

ARTICLE INFO

Article history:

Received 2 December 2017

Received in revised form 6 June 2018

Accepted 11 June 2018

Available online 26 June 2018

Keywords:

Topology optimization

Electroosmosis

Electrode

Micromixer

ABSTRACT

In confined microfluidic spaces such as microchannels, electroosmosis is a convenient Coulomb-force mechanism used to electrically actuate charged particles and ions presented in the fluid and pump the electrolytic fluid itself through drag forces. The shape and position of electrode pairs, whose induced charges are in contact with the fluid, determine the electric field and hence the resulting fluid-dynamic velocity distribution. In this paper, we address the inverse design of the electrode-pair patterns in such actuation mechanisms. Our approach is to use topology optimization to inversely determine the patterns of an electrode pair. The optimization procedure requires a mathematical description of the desired fluid behaviour, and then drives the patterns of the electrode pairs to achieve the goal performance. We demonstrate the behaviour of the procedure, which couples the Navier-Stokes equations with charge transportation, to implement an efficient electroosmotic micromixer for laminar microflow. We show that the procedure allows to investigate such microflows under the influence of selected parameter variations, thereby exploring the design space towards optimal device performance. This developed method is novel on the topology optimization of a surface structure to control bulk performance and its implementation over a lower-dimensional surface of an otherwise volumetric domain, where the material interpolation is implemented between Dirichlet and Neumann types of boundary conditions.

© 2018 Elsevier Ltd. All rights reserved.

1. Introduction

The lab-on-a-chip approach has brought about a paradigm shift in orchestrating fluid laboratory operations, providing high yield in a confined space combined with high flexibility for experiments in biology and chemistry [1–3]. In microfluidics, it is often necessary to move fluids from one part of the device to another, to control fluid flow, enhance mixing, and separate fluid constituents, to name the most important unit operations. Electroosmosis, particularly suitable for microfluidic devices, provides an attractive approach for manipulating liquids in microdevices, since the microdevices operating on this principle do not require any moving parts. In this context, electroosmosis has been investigated in

several reports as a primary mover, typically focusing on electroosmotic micromixers [4,5] and electroosmotic pumping [6–8].

Electroosmosis is caused by the accumulation of net electric charges on a solid surface that is in contact with an electrolyte solution [9,10]. As a result, charges concentrate in the thin liquid layer next to the solid surface. This thin layer is known as the Debye (or double) layer, and its thickness typically has a magnitude of 10 nm [9]. Away from the solid surface, the electrolyte is neutral. The charge separation next to the solid wall causes either a positive or negative potential difference (i.e. Zeta potential) across the Debye layer. The magnitude of the Zeta potential depends on the characteristics of both the solid and liquid. In the presence of an external electric field, the charges trapped in the double layer are attracted to the opposite electrode and drag the liquid along in this direction. Therefore, the electric field creates a body force that induces fluid motion, through its action on the charges, as sketched in Fig. 1. Usually, the Debye layer is much smaller than the characteristic size of a typical microfluidic

* Corresponding authors.

E-mail addresses: dengyb@ciomp.ac.cn (Y. Deng), jan.korvink@kit.edu (J.G. Korvink).

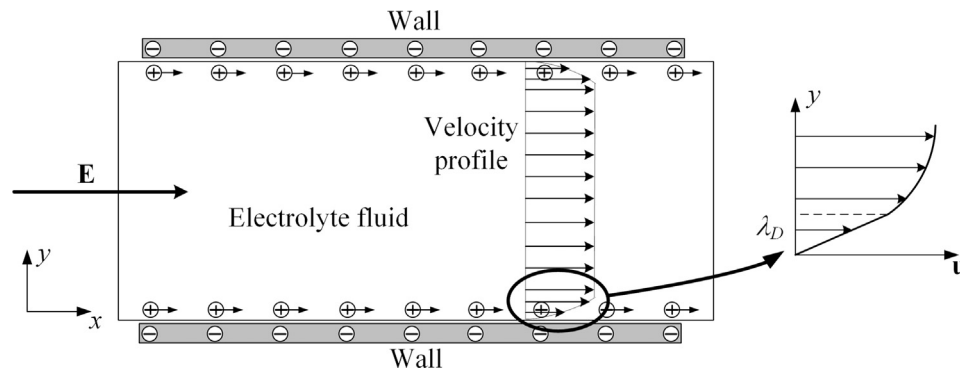


Fig. 1. Sketch for electroosmosis in a microchannel, where E is the electric field, λ_D is the thickness of the Debye layer, and u is the velocity.

channel, so that the fluid dynamics in the thin Debye layer can be approximated to be a slip wall with slipping velocity proportional to the tangential component of the external electric field. As a result, the electrode patterns on the walls of the microchannel play a dominant role on the microfluidic performance of electroosmotic actuation.

Several reports consider the mathematical modelling of electroosmosis-like electrodynamic microflows by analytical, numerical and experimental approaches [4,11–16]. The most relevant studies consider Joule heating effects [17,18]; the implementation of shape optimization-based geometrical design of electroosmotic microchannel [19,20]; the optimization of the zeta potential distribution for minimal dispersion in an electroosmotic microchannel [21]; and topology optimization of a dielectric solid for induced-charge electroosmotic flow [22]. In these reports, electrodes play the dominant role in generating the microfluidic motion due to their ability to induce an external electric field with attracting charges. Therefore, reasonable patterns of a electrode pair are a key for achieving the desired performance of an electrokinetic microflow. Then, asymmetric polarization and nonplanar patterns have been adopted for electroosmotic actuation [23,24]; a staggered array of electrodes has been utilized to produce electroosmotic vortices for micromixing [25]; an asymmetric electrode pair has been used in an electroosmotic microconcentrator [26]; an electric potential effect imposed on the wall electrodes has been discussed for binary fluids [27]; facing rows of electrodes have been used for remediation of polluted soils by electrokinetic soil flushing [28], to name the most recent reports. Although several relevant results provided insight into the control of electroosmosis, limits on determining the exact electrode patterns still exist in view of design methods lacking generality, flexibility and efficiency, mainly because of the remaining dependence on a designers' intuition. Therefore, this paper focuses on a flexible topology optimization method for the electrode patterns of electroosmotic microfluidics to overcome these limits.

Topology optimization is currently regarded to be the most robust methodology for the inverse determination of material distributions in structures that meet given structural performance criteria [29]. The optimal topology of structures was investigated already as early as 1904 for trusses by Michell, and this resulted in structure types carrying his name [30]. The method has been developed for elasticity by Bendsøe and Kikuchi [31], and then was extended to a variety of application areas, e.g. acoustics, electromagnetics, fluid dynamics and thermodynamics [32–59], to list the most prominent. As a layout optimization method, topology optimization can improve the shape and topology of structures simultaneously, whereas shape optimization determines the

performance of a device by adjusting the positions of structural boundaries only, therefore retaining the original topology of the structure. Therefore, topology optimization is more general. Currently, the density method [50,51], and level set method [60–63], have been widely used to describe the material distribution in topology optimization. The density method was first used to design stiffness and compliance mechanisms [31–33], but has been extended to multiple physical problems, such as acoustic, electromagnetic, fluidic, optical and thermal problems [29,34,48,49,52,53,57]. For fluidic problems, it was first considered for Stokes flows [57,64,65] and Darcy-Stokes flows [56,66]; it was later extended to Navier-Stokes flows [55,67–70], non-Newtonian flows [71], unsteady flows [54,59,72], flows with body forces [73,74], and two-phase flow with immiscible interfaces [75]; it has also been applied to design fluidic devices [76–81]. The level set method, pioneered by Osher and Sethian [82], accomplishes a change of topology by evolving and merging the zero contour of the level set function, i.e., embedding the boundary in a higher dimension. This method provides a general approach to track the implicit interface between two phases, and it has been applied to fluidic shape and topology optimization [55,70,83,84]. One of the major advantages of the level set method lies in expressing continuously moving interfaces, and abstracting the material domains that correspond to the structural topology. Compared to the level set method, the density method has the merits of rapid and robust convergence, weak dependence on the initial distribution of the design variable, and the ability to deal with multiple constraints. It is therefore our method of choice for the current paper.

The conventional approach for topology optimization in fluid dynamics considers the bulk topology of the flow region, instead of considering a boundary approach that would reside in a lower dimension of the computational domain [85]. For electroosmosis, the flow channel topology will not be modified, but rather the electrode patterns will be inversely designed. In the paper we described the inverse design of electrode patterns by implementing an interpolation of the electric insulation and electric potential on specified walls of microchannels; our method can therefore also be regarded to be the first attempt to inversely determine a structural topology at lower dimension than the computational domain.

The capability of our optimization method for electrode patterns is demonstrated by determining the electrodes for electroosmotic micromixers, because electroosmosis is particularly effective in this research area. Microflow is usually associated with a highly ordered laminar flow, and the lack of turbulence makes diffusion to be the primary mechanism for mixing. While diffusive mixing of small molecules can occur in a matter of

seconds over lengths of tens of micrometers, mixing of larger molecules require equilibration times from minutes to hours over comparable lengths. Such delays are impractically long for many chemical analyses. These problems have led to an intensification of research efforts towards more efficient micromixers in microfluidics [86]. Most micromixers are either passive based on geometrical stirring, or active with requiring moving parts or external forces (e.g. pressure or electric field) [86]. In a passive micromixer, the ways of increasing the mixing are equivalent to shredding two or several fluids into very thin alternating layers, which decreases the average diffusion length for the molecules between two different fluids. However, these devices usually require long mixing channels, because different fluids often run in parallel. Another way of improving mixing efficiency is to use active micromixers with moving parts that stir the fluids. At the microscale, moving parts in an active mixer are very fragile. One efficient alternative is to use electroosmosis to achieve a mixing effect that is perpendicular to the main direction of the microflow [4,87]. Therefore, we consider the inverse design of electrode patterns for electroosmotic micromixers, to demonstrate the capability of the presented method.

Our computed results show that complete micromixing of microflows can be achieved over relatively short lengths by electrodes with customized design patterns. In the following, an electroosmotic micromixer is modeled using the topology optimization method in Section 2; the variational problem for the electrode patterns is analyzed and solved in Section 2; the solution procedure for the variational problems is introduced in Section 3; the computed results are discussed in Section 4; the paper is concluded in Section 5. All mathematical descriptions in the paper are provided in the Cartesian coordinate system.

2. Modelling

To demonstrate the capability of our method, a direct-current (DC) electroosmotic micromixer with electrodes on its walls is modelled. In this electroosmotic micromixer, a fluid flux is imposed on the inlet with known concentration distribution, the anode and cathode actuating the electroosmosis are localized on the ceiling and floor surfaces to produce the secondary flow perpendicular to the main direction of the microflow and achieve a mixing effect (Fig. 2a). In the DC case, the asymmetry between the anode on the ceiling and cathode on the floor can result in the existence of the tangential component of the electric field in the electrical double layer (EDL). And this tangential electric field

further imposes a body force on the fluid in the EDL and induces the fluid velocity (Fig. 2b).

In electroosmosis, the electric potential can be decomposed into an external electric potential due to the imposition of the externally applied electrode potential and an electric potential due to surface wall charge [88]. Therefore, the body force imposed on the fluid is the electric force of these two potentials. Under the continuum hypothesis, the Navier-Stokes equations, including an electrical driving body force term to represent the interaction between the excess ions of the EDL and the external electric field induced by the electrode potential, is used to describe the electroosmotic flow, where the wall boundaries are of no-slip type and an assumption is made that the Joule heating effect is negligible [89]:

$$\begin{aligned} \rho \mathbf{u} \cdot \nabla \mathbf{u} + \nabla \cdot [-\eta(\nabla \mathbf{u} + \nabla \mathbf{u}^T) + p\mathbf{I}] &= \frac{\epsilon_r \epsilon_0}{\lambda_D^2} \psi \nabla V, \text{ in } \Omega \\ -\nabla \cdot \mathbf{u} &= 0, \text{ in } \Omega \\ \mathbf{u} &= \mathbf{0}, \text{ on } \Gamma_w \end{aligned} \tag{1}$$

where \mathbf{u}, p are the fluid velocity and pressure, respectively; \mathbf{I} is the unit tensor; ρ and η are the density and dynamic viscosity of the electrolyte solution, respectively; λ_D is the Debye length, and it is the characteristic thickness of the EDL for a given solid-electrolyte liquid interface; ϵ_r and ϵ_0 are the relative permittivity of the electrolyte solution and permittivity of free space, respectively; ψ is the electric potential due to surface wall charge; V is the external electric potential imposed by the electrodes; Ω is the computational domain sketched in Fig. 2, with the inlet boundary Γ_i , wall boundary $\Gamma_w = \Gamma_{wa} \cup \Gamma_{de}$ and outlet boundary Γ_o satisfying $\Gamma_i \cup \Gamma_o \cup \Gamma_w = \partial\Omega$.

Within the EDL, the electrical potential drops from the zeta potential to zero [9,89]. The ion distribution in the EDL is determined primarily by the zeta potential, and the corresponding potential distribution due to surface wall charge can be obtained by solving the equation

$$\begin{aligned} \nabla^2 \psi &= \frac{1}{\lambda_D^2} \psi, \text{ in } \Omega \\ \psi &= -\zeta, \text{ on } \Gamma_w \\ \mathbf{n} \cdot \nabla \psi &= 0, \text{ on } \Gamma_i \cup \Gamma_o \end{aligned} \tag{2}$$

where \mathbf{n} is the outward unit normal on $\partial\Omega$. For a symmetrical and univalent electrolyte at room temperature, the Debye length of the EDL is on the magnitude 10 nm for a concentration of 10^{-3} M. In micro scale, it is very small compared to the characteristic length

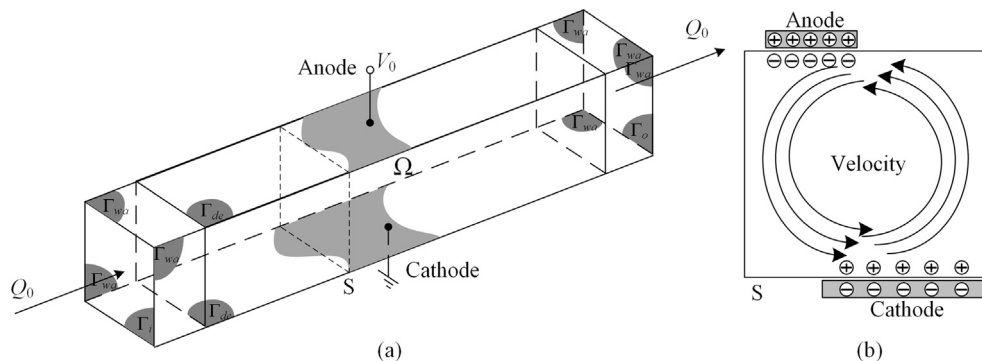


Fig. 2. (a) Sketch of the computational domain Ω for an electroosmotic micromixer, where Γ_i is the inlet, Γ_o is the outlet, Γ_w composed of Γ_{wa} and Γ_{de} is the wall of microchannel, Q_0 is the fluid flux imposed on the inlet of the microchannel, V_0 is the electrical potential imposed on the anode, the cathode is connected to ground, the electrode patterns are determined on Γ_{de} , and S is one cross-section of the electroosmotic micromixer; (b) demonstration for the secondary flow in the cross-section S .

of the microchannel [9]. This results in the high-resolution mesh for the EDL discretisation and heavy computation cost in the numerical computation of electroosmosis; especially, these problems are definitive in the three-dimensional numerical computation. To avoid such problems caused by the multi-scale physics of electroosmosis, the Helmholtz-Smoluchowski relation has been widely used to remove the body force term of the Navier-Stokes equations by approximating the EDLs to be slip walls, with the fluid velocity proportional to the tangential component of the electric field intensity [11]. Therefore, based on such a thin double layer approximation, Eqs. (1) and (2) can be replaced to be

$$\begin{aligned} \rho \mathbf{u} \cdot \nabla \mathbf{u} + \nabla \cdot [-\eta(\nabla \mathbf{u} + \nabla \mathbf{u}^T) + p\mathbf{I}] &= \mathbf{0}, \text{ in } \Omega \\ -\nabla \cdot \mathbf{u} &= 0, \text{ in } \Omega \\ \mathbf{u} &= -\mu_{eo}[\nabla V - (\mathbf{n} \cdot \nabla V)\mathbf{n}], \text{ on } \Gamma_w \end{aligned} \quad (3)$$

where $\mu_{eo} = -\epsilon_r \epsilon_0 \zeta_0 / \eta$ is the electroosmotic mobility, with ζ_0 representing the Zeta potential. This Zeta potential can be determined by a full model, i.e. the three capacitor model that has been provided in the Refs. [90–92].

For the computational domain of the electroosmotic microflow, the inlet and outlet boundaries are used to truncate the microchannel from its system or network. Because of the thin double layer approximation with the Helmholtz-Smoluchowski relation which approximates the EDLs to be slip walls, slip velocity can exist at the intersection between the inlet and walls of the computational domain. This comes in conflict with the typically-used parabolic velocity distribution with no-slip velocity at the sides of the inlet. A defective boundary condition has non-essence to enforce the velocity distribution on the corresponding boundary [93,94]. Therefore, the defective boundary condition is imposed on the inlet of the electroosmotic microflow with a specified flux, to avoid the conflict:

$$\int_{\Gamma_i} -\mathbf{u} \cdot \mathbf{n} d\Gamma = Q_0, \text{ on } \Gamma_i, \quad (4)$$

where $Q_0 = U \int_{\Gamma_i} 1 ds$ is the know flux at the inlet Γ_i , and U is the average velocity. At the outlet, an open boundary condition can be imposed as

$$[-\eta(\nabla \mathbf{u} + \nabla \mathbf{u}^T) + p\mathbf{I}] \cdot \mathbf{n} = \mathbf{0}, \text{ on } \Gamma_o \quad (5)$$

For electroosmotic micromixers, the two factors that influence the mixing performance are diffusion and chaotic advection. The mixing of two species diluted in the electroosmotic microflows can be described by the convection-diffusion equation

$$\mathbf{u} \cdot \nabla c - \nabla \cdot (D\nabla c) = 0, \text{ in } \Omega, \quad (6)$$

where c is the concentration, and D is the diffusion constant. The imposed boundary conditions for the convection-diffusion equation are the known concentration distribution at the inlet

$$c = c_i(\mathbf{x}), \text{ on } \Gamma_i, \quad (7)$$

and the diffusion insulation at the wall and outlet

$$-(D\nabla c) \cdot \mathbf{n} = 0, \text{ on } \Gamma_w \cup \Gamma_o, \quad (8)$$

where c_i is the known concentration distribution at the inlet of the electroosmotic micromixer.

The distribution of the external electrical potential in the electroosmotic micromixer can be derived by the Laplace equation

$$-\nabla \cdot (\sigma \nabla V) = 0, \text{ in } \Omega, \quad (9)$$

where σ is the electric conductivity. As sketched in Fig. 2, the wall boundary Γ_w is split into two parts, Γ_{wa} and Γ_{de} . For the external electrical potential, Γ_{wa} is an electric insulation boundary with $-(\sigma \nabla V) \cdot \mathbf{n} = 0$; the design domain for the electrodes Γ_{de} is the

union of the electric insulation and electric potential boundary parts. To distinguish those two types of boundary, a variable denoted physical density is utilized; it takes on values in the range [0, 1], with 0 and 1 respectively representing electric potential and electric insulation boundary types. The boundary condition on Γ_{de} can then be expressed as an interpolation of electric potential and electric insulation

$$-(\sigma \nabla V) \cdot \mathbf{n} = \alpha(V - V_0), \text{ on } \Gamma_{de}, \quad (10)$$

where V_0 is the specified electric potential on the electrodes, and α is the penalization expressed to be [57]

$$\alpha = \alpha_{max} \frac{q(1 - \gamma_{fp})}{q + \gamma_{fp}}, \quad (11)$$

with γ_{fp} , α_{max} and q respectively representing the physical density variable, the penalization parameter, and the parameter used to tune the convexity of the penalization. The value of α_{max} should be chosen to be large enough to ensure the domination of the term $(V - V_0)$ in Eq. (10), when the physical density takes on the value 0. Meanwhile, Eq. (10) degenerates into the electric insulation boundary condition, when the physical density takes on the value 1. Based on numerical tests, α_{max} and q are chosen to be 1×10^5 and 1×10^{-3} , respectively. The electric insulation boundary condition is imposed on the inlet, outlet, and the left walls of the electroosmotic microflows

$$-(\sigma \nabla V) \cdot \mathbf{n} = 0, \text{ on } \Gamma_i \cup \Gamma_o \cup \Gamma_{wa}. \quad (12)$$

The physical density variable in Eq. (11) is computed from a design variable defined on Γ_{de} , using the procedure introduced in [95]: the design variable is modified using a Helmholtz filter to ensure a minimum scale of the implicitly expressed pattern

$$\begin{aligned} -r^2 \nabla_s \cdot \nabla_s \gamma_f + \gamma_f &= \gamma, \text{ in } \Gamma_{de}, \\ -r^2 \nabla_s \gamma_f \cdot \mathbf{n}_s &= 0, \text{ on } \partial \Gamma_{de}, \end{aligned} \quad (13)$$

where γ is the design variable, and γ_f is the filtered design variable; ∇_s is the gradient operator defined for the local coordinate system on Γ_{de} ; r is the filter radius, and is used to control the feature size of the electrode patterns; \mathbf{n}_s is the outward unit normal on $\partial \Gamma_{de}$. After filtering, the filtered design variable is projected using the threshold method to remove intermediary values between 0 and 1 and to derive the physical density

$$\gamma_{fp} = \frac{\tanh(\beta \xi) + \tanh(\beta(\gamma_f - \xi))}{\tanh(\beta \xi) + \tanh(\beta(1 - \xi))}, \quad (14)$$

where β and ξ are the projection parameters. For the choice of the projection parameters, one can refer to [96].

The following task is to solve for the optimal 0 – 1 distribution of the physical density, which implicitly defines the electrode patterns, using a variational problem constructed by the topology optimization approach. For a micromixer used to mix two fluids with different solutes, the desired effect is achieved when a spatially averaged concentration value is found at the outlet of the device. The mixing performance can be evaluated mathematically through the normalized least square variance between the obtained concentration and the anticipated concentration at the outlet, and in which the normalizing factor is the least square difference between the concentration distribution at the inlet and the anticipated concentration at the outlet [80,98,99]. The design target is to find reasonable electrode patterns that can achieve the highest degree of mixing corresponding to the lowest mixing evaluation. Therefore, a variational problem is constructed as follows:

Find $\gamma_{fp}(\mathbf{x}) \in \{0, 1\}$ with $\gamma(\mathbf{x}) \in [0, 1]$ for $\forall \mathbf{x} \in \Gamma_{de}$,

to minimize $\Psi = \frac{1}{\Psi_0} \int_{\Gamma_o} (c - \bar{c})^2 ds$ with $\Psi_0 = \int_{\Gamma_i} (c_i - \bar{c})^2 ds$,

constrained by

$$\left\{ \begin{array}{l} \left\{ \begin{array}{l} -\nabla \cdot (\sigma \nabla V) = 0, \text{ in } \Omega \\ -(\sigma \nabla V) \cdot \mathbf{n} = 0, \text{ on } \Gamma_i \cup \Gamma_o \cup \Gamma_{wa} \text{ (External Electrical Potential)} \\ -(\sigma \nabla V) \cdot \mathbf{n} = \alpha (V - V_0), \text{ on } \Gamma_{de} \end{array} \right. \\ \left\{ \begin{array}{l} \rho \mathbf{u} \cdot \nabla \mathbf{u} + \nabla \cdot [-\eta (\nabla \mathbf{u} + \nabla \mathbf{u}^T) + p \mathbf{I}] = \mathbf{0}, \text{ in } \Omega \\ -\nabla \cdot \mathbf{u} = 0, \text{ in } \Omega \\ \int_{\Gamma_i} -\mathbf{u} \cdot \mathbf{n} d\Gamma = Q_0, \text{ on } \Gamma_i \quad \text{(Navier-Stokes Equations)} \\ [-\eta (\nabla \mathbf{u} + \nabla \mathbf{u}^T) + p \mathbf{I}] \mathbf{n} = \mathbf{0}, \text{ on } \Gamma_o \\ \mathbf{u} = -\mu_{eo} [\nabla V - (\mathbf{n} \cdot \nabla V) \mathbf{n}], \text{ on } \Gamma_w \end{array} \right. \\ \left\{ \begin{array}{l} \mathbf{u} \cdot \nabla c - \nabla \cdot (D \nabla c) = 0, \text{ in } \Omega \\ c = c_i(\mathbf{x}), \text{ on } \Gamma_i \quad \text{(Convection-Diffusion Equation)} \\ -(D \nabla c) \cdot \mathbf{n} = 0, \text{ on } \Gamma_w \cup \Gamma_o \end{array} \right. \\ \left\{ \begin{array}{l} -r^2 \nabla_s \cdot \nabla_s \gamma_f + \gamma_f = \gamma, \text{ in } \Gamma_{de} \\ -r^2 \nabla_s \gamma_f \cdot \mathbf{n}_s = 0, \text{ on } \partial \Gamma_{de} \end{array} \right. \text{ (Helmholtz Filter)} \\ \gamma_{fp} = \frac{\tanh(\beta \xi) + \tanh(\beta(\gamma_f - \xi))}{\tanh(\beta \xi) + \tanh(\beta(1 - \xi))} \text{ (Threshold Projection)} \end{array} \right. \quad (15)$$

where Ψ_0 is the least square variance between the obtained concentration and the anticipated concentration at the inlet, and ds is the differential on $\partial \Omega$.

3. Analyzing and solving

The variational problem is solved using an iterative approach, for which the design variable is evolved towards optimality according to gradient information extracted from the variational problem in Eq. (15). The gradient information is determined via adjoint analysis of the variational problem.

By the adjoint method for a partial differential equation constrained optimization problem [100], the variational problem is analyzed, based on weak forms of the adjoint equations for the convection-diffusion equation, Navier-Stokes equations, Laplace equation, and Helmholtz filter (details are supplied by Appendix A):

1. Find $c_a \in \mathcal{H}(\Omega)$ and $\lambda_{ca} \in \mathcal{H}^{-\frac{1}{2}}(\Gamma_i)$ satisfying:

$$\begin{aligned} & \int_{\Omega} \mathbf{u} \cdot \nabla \hat{c}_a c_a + D \nabla c_a \cdot \nabla \hat{c}_a dv \\ & + \sum_{i=1}^{N_e} \int_{\Omega_i} \tau_{supg}(\mathbf{u} \cdot \nabla c_a) (\mathbf{u} \cdot \nabla \hat{c}_a - D \nabla^2 \hat{c}_a) dv \\ & + \int_{\Gamma_i} \lambda_{ca} \hat{c}_a + c_a \hat{\lambda}_{ca} ds + \frac{1}{\Psi_0} \int_{\Gamma_o} 2(c - \bar{c}) \hat{c}_a ds \\ & = 0, \quad \forall \hat{c}_a \in \mathcal{H}(\Omega) \text{ and } \forall \hat{\lambda}_{ca} \in \mathcal{H}^{\frac{1}{2}}(\Gamma_i); \end{aligned} \quad (16)$$

2. Find $\mathbf{u}_a \in (\mathcal{H}(\Omega))^3$, $p_a \in \mathcal{L}^2(\Omega)$, $\lambda_{fa} \in (\mathcal{H}^{-\frac{1}{2}}(\Gamma_w))^3$ and $\lambda_{qa} \in \mathbb{R}$ satisfying:

$$\begin{aligned} & \int_{\Omega} \rho [(\hat{\mathbf{u}}_a \cdot \nabla \mathbf{u}) \cdot \mathbf{u}_a + (\mathbf{u} \cdot \nabla \hat{\mathbf{u}}_a) \cdot \mathbf{u}_a] + \nabla \mathbf{u}_a : [\eta (\nabla \hat{\mathbf{u}}_a + \nabla \hat{\mathbf{u}}_a^T) \\ & - \hat{p}_a \mathbf{I}] - p_a \nabla \cdot \hat{\mathbf{u}}_a + \hat{\mathbf{u}}_a \cdot \nabla c c_a dv \\ & + \sum_{i=1}^{N_e} \int_{\Omega_i} -\tau_{gls} \nabla p_a \cdot \nabla \hat{p}_a + \left(\frac{\partial \tau_{supg}}{\partial \mathbf{u}} \cdot \hat{\mathbf{u}}_a \right) (\mathbf{u} \cdot \nabla c_a) (\mathbf{u} \cdot \nabla c - D \nabla^2 c) \\ & + \tau_{supg}(\hat{\mathbf{u}}_a \cdot \nabla c_a) (\mathbf{u} \cdot \nabla c - D \nabla^2 c) \\ & + \tau_{supg}(\mathbf{u} \cdot \nabla c_a) (\hat{\mathbf{u}}_a \cdot \nabla c) dv + \int_{\Gamma_i} \hat{\lambda}_{qa} \mathbf{u}_a \cdot \mathbf{n} + \lambda_{qa} \hat{\mathbf{u}}_a \cdot \mathbf{n} ds \\ & + \int_{\Gamma_w} \lambda_{fa} \cdot \hat{\mathbf{u}}_a + (\hat{\lambda}_{fa} - \hat{p}_a \mathbf{n}) \cdot \mathbf{u}_a ds = 0, \\ & \forall \hat{\mathbf{u}}_a \in (\mathcal{H}(\Omega))^3, \quad \forall \hat{p}_a \in \mathcal{L}^2(\Omega), \quad \forall \hat{\lambda}_{fa} \in (\mathcal{H}^{\frac{1}{2}}(\Gamma_w))^3 \text{ and } \forall \hat{\lambda}_{qa} \in \mathbb{R}; \end{aligned} \quad (17)$$

3. Find $V_a \in \mathcal{H}(\Omega)$ satisfying:

$$\begin{aligned} & \int_{\Omega} \sigma \nabla V_a \cdot \nabla \hat{V}_a dv + \int_{\Gamma_{de}} \alpha V_a \hat{V}_a ds \\ & + \int_{\Gamma_w} \mu_{eo} [\nabla \hat{V}_a - (\mathbf{n} \cdot \nabla \hat{V}_a) \mathbf{n}] \cdot \lambda_{fa} ds = 0, \quad \forall \hat{V}_a \in \mathcal{H}(\Omega); \end{aligned} \quad (18)$$

4. Find $\gamma_{fa} \in \mathcal{H}(\Gamma_{de})$ satisfying:

$$\begin{aligned} & \int_{\Gamma_{de}} r^2 \nabla_s \hat{\gamma}_{fa} \cdot \nabla_s \hat{\gamma}_{fa} + \gamma_{fa} \hat{\gamma}_{fa} + (V - V_0) V_a \frac{\partial \alpha}{\partial \gamma_{fp}} \frac{\partial \gamma_{fp}}{\partial \gamma_f} \hat{\gamma}_{fa} ds \\ & = 0, \quad \forall \hat{\gamma}_{fa} \in \mathcal{H}(\Gamma_{de}); \end{aligned} \quad (19)$$

where λ_f and λ_Q are the Lagrangian multipliers used to impose the velocity boundary condition and defective boundary condition on Γ_w and Γ_i for the Navier-Stokes equations; λ_c is the Lagrangian multiplier used to impose the known concentration boundary condition on Γ_i for the convection-diffusion equation; $c_a, \mathbf{u}_a, p_a, V_a$ and γ_{fa} are the adjoint variables of the corresponding state variables; λ_{fa} and λ_{Qa} are the adjoints of the Lagrangian multiplier λ_f and λ_Q ; λ_{ca} is the adjoint of the Lagrangian multiplier λ_c ; $\hat{c}_a, \hat{\mathbf{u}}_a, \hat{p}_a, \hat{V}_a, \hat{\gamma}_{fa}, \hat{\lambda}_{fa}$ and $\hat{\lambda}_{ca}$ are the test functions of the corresponding adjoint variables; $\mathcal{H}(\Omega)$ and $\mathcal{L}^2(\Omega)$ are the first-order Hilbert space and the second-order Lebesgue integrable functional space defined on Ω ; $\mathcal{H}^{-1/2}(\Gamma_w)$ is the dual space of the trace space $\mathcal{H}^{1/2}(\Gamma_w)$; $\mathcal{H}(\Gamma_{de})$ is the first-order Hilbert space defined on Γ_{de} ; \mathbb{R} is the real number field; to solve the partial differential equations corresponding to the constraints of Eq.(15), a linear element-based finite element method is utilized, with the Navier-Stokes equations and convection-diffusion equation stabilized using the generalized least squares (GLS) and streamline upwind Petrov-Galerkin (SUPG) technologies [101]; N_e represents the number of finite elements used to discretize Ω ; τ_{gls} and τ_{supg} are the stabilization parameters chosen as in [101]:

$$\tau_{gls} = \frac{h_i^2}{12\eta},$$

$$\tau_{supg} = \left(\frac{4}{h_i^2 D} + \frac{2|\mathbf{u}|}{h_i} \right)^{-1},$$
(20)

with h_i representing the size of the i -th element Ω_i . The first-order adjoint derivative of the variational problem in Eq. (15) is

$$\delta\hat{\Psi} = \int_{\Gamma_{de}} -\gamma_{fa} \delta\gamma ds, \quad \forall \delta\gamma \in \mathcal{L}^2(\Gamma_{de}),$$
(21)

where $\hat{\Psi}$ is the augmented Lagrangian corresponding to the variational problem in Eq. (15); $\delta\hat{\Psi}$ and $\delta\gamma$ are the first-order variational of the augmented Lagrangian and design variable; $\mathcal{L}^2(\Gamma_{de})$ is the second-order Lebesgue integrable functional space defined on Γ_{de} . In Eq. (21), γ_{fa} is obtained by sequentially solving the Eqs. (16)–(19). Subsequently, the adjoint derivative is used to evolve the design variable.

After adjoint analysis, an iterative procedure that covers the following steps can be used to solve the variational problem (Fig. 3):

- (a) The PDE constraints are solved with the current design variable;
- (b) The adjoint equations are solved based on the solution of the PDE constraints;
- (c) The adjoint derivative of the optimization objective function is computed;
- (d) The design variable is updated using the method of moving asymptotes (MMA) [102];
- (e) The convergence criterion is checked. If not satisfied, the procedure will return to (a), else the procedure is terminated.

For convergence, either the change of the objective function values in five consecutive iterations satisfies $1/5 \sum_{i=0}^4 |\Psi_{k-i} - \Psi_{k-1}| / |\Psi_k| \leq 1 \times 10^{-3}$ in the k -th iteration step, or the maximal iteration number 240 has been reached, where Ψ_k is the objective function value in the k -th iteration.

In this iterative procedure, the threshold parameter ξ in Eq. (14) is set to 0.5; the initial value of the projection parameter β is set to

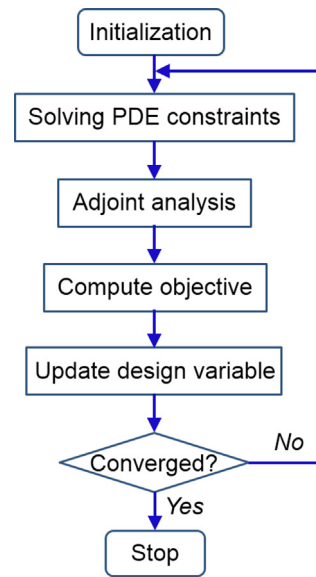


Fig. 3. Flowchart for the iterative procedure used to solve the variational problem in Eq. (15).

1, and is doubled after every 40 iterations, until a preset maximal value of 32 is reached; the finite element solution of all partial differential equations and corresponding adjoint equations is implemented using the finite element software COMSOL Multiphysics (<http://www.comsol.com>). Discretization is performed using linear cubic elements for all spatially distributed variables. More details on the relevant programming parameters are found in [59,68].

4. Results and discussion

In this section we report our exploration of the new capability, by considering a fluidic microchannel of square cross-section, and with a cathode on its floor and an anode attached to the ceiling. An electrolyte with density $\rho = 1 \times 10^3$ kg/m³, dynamic viscosity $\eta = 1 \times 10^{-3}$ Pa·s, dielectric constant $\epsilon_r = 80.2$, conductivity $\sigma = 0.12$ ($\Omega \cdot \text{m}$)⁻¹, and Zeta potential $\zeta_0 = -0.1$ V flows in the channel. The Zeta potential reflects the choice of channel material.

The characteristic size of the cross-section of the computational domain sketched in Fig. 2 is set to be l , so that the length of the microchannel covered by the electrodes is defined by $n_l \cdot l$ with n_l representing the fold number. The length of the inlet and outlet of the design domain is also equal to l , so as to remove the influence of the entry conditions at the electrodes. The computational domain is discretized by $20 \times 20 \times 20 = 8000$ brick elements per l^3 sector. $h_e = l/20$ denotes the size of a finite element. The design domain is set to be the floor and ceiling surfaces of the channel demonstrated in Fig. 2.

For micromixing, diffusion alone is inefficient. Moving fluids can greatly enhance mixing through chaotic advection in which the region containing the impurities is strongly deformed; the interface between the impurities grows exponentially, and diffusion becomes efficient. Therefore, the two physical processes that implement mixing in a micromixer are diffusion and chaotic advection [86,97]. The relative importance of these two factors can be measured by the dimensionless Péclet number, calculated from $Pe = Ul/D$ with U representing the averaged velocity at the inlet. When the Péclet number satisfies $Pe \gg 1$, the main mixing factor is the fluidic convection. Otherwise, the main factor is the diffusion. The convection intensity of the flow is characterised by the Reynolds number, calculated from $Re = \rho Ul/\eta$. When $Re \gg 1$,

convection dominates the flow; otherwise, viscosity dominates it. In microfluidics, the typical magnitudes of a sample volume, characteristic size of microchannels are 1 μL and 100 μm , respectively; the typical sample is aqueous solution with density, dynamic viscosity and diffusion constant in 10^3 kg/m^3 , $10^{-3} \text{ Pa}\cdot\text{s}$ and $10^{-8} \text{ m}^2/\text{s}$, respectively. Then, the typical values of Péclet number and Reynolds number are 10^3 and 10, for the microflows in microfluidic chips. And these values have been widely used in the researches reviewed in [86].

After selecting the parameters as listed in Table 1, the variational problem in Eq. (15) is solved iteratively. Snapshots for the evolution of the physical density variable and associated convergence history of the optimization objective function are shown in Fig. 4 and 5. From these, the robustness of the topology optimization method is confirmed by inspection. In the evolution history, the symmetry of the physical density is broken; such symmetry-break can avoid the counteract of the electroosmotic action in the cross-section of the micromixer and achieve the mixing-

Table 1
Parameters used for solving the variational problem in Eq. (15). Here h_e is the size of the finite elements used to discretize the computational domain.

Parameter	V_0	n_l	Pe	Re	r	l
Value	5 V	6	1×10^3	10	$2h_e$	400 μm

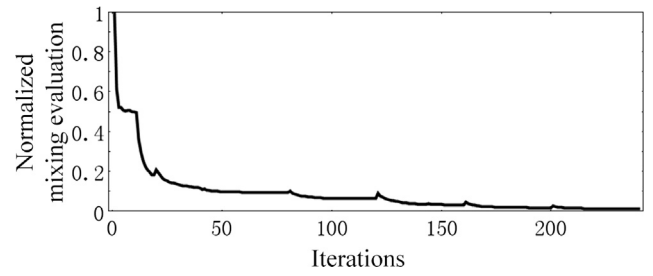


Fig. 5. Convergence history of the optimization objective function values, which are normalized by a measure computed from the initial distribution of the design variable.

performance evolution corresponding to the convergent history of the objective function. The final electrode patterns are shown in Fig. 6a, including the distribution of the streamlines in the micromixer. The electrode patterns generate a tangential velocity at the walls of the micromixer (Fig. 6b); this can effectively swirl the streamlines (Fig. 6a) and enhance the chaotic advection of the microflow by inducing secondary flows in the cross-sections (Fig. 6c); the enhanced advection distorts the interface between the two fluids, as shown in Fig. 6d. By inspecting the concentration distribution at the outlet, we surmise that complete mixing is achieved over a length of 2.4mm, or six folds of the channel width. In Fig. 6, the derived electrode patterns stir the moving fluids,

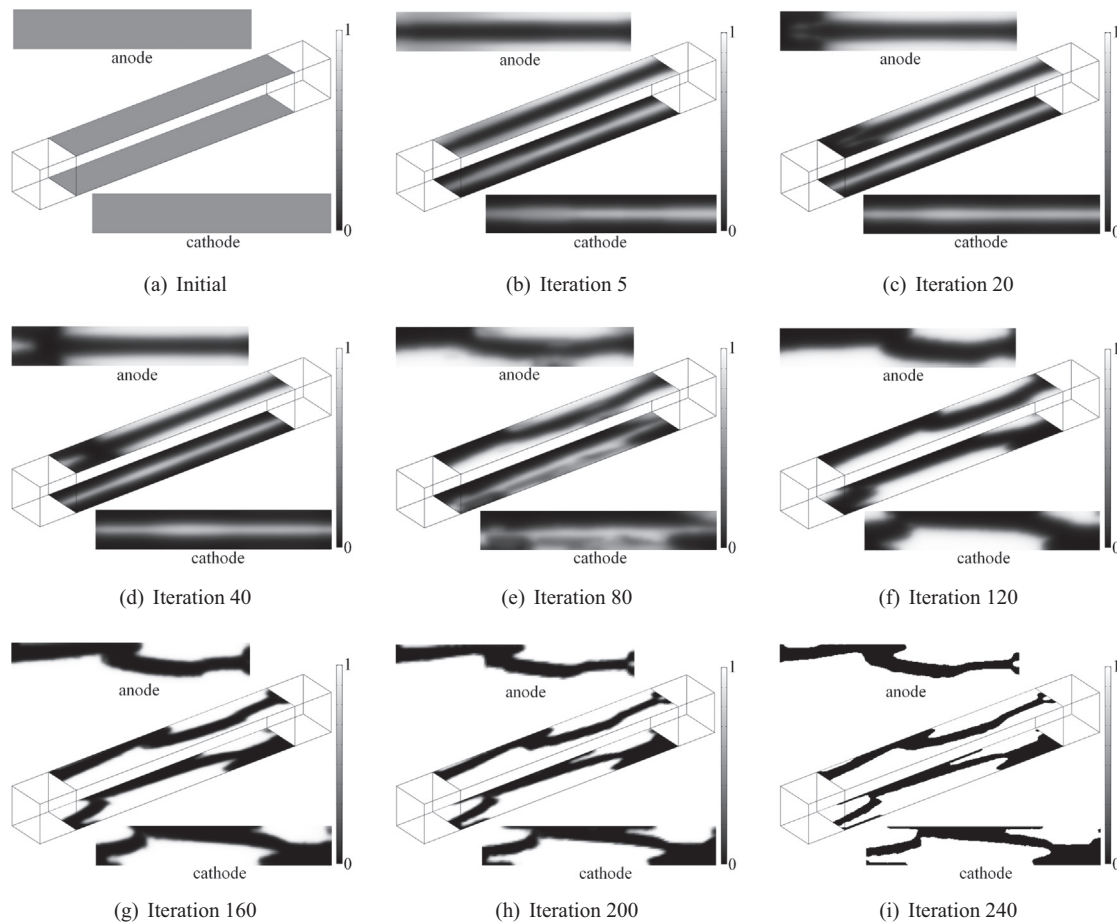


Fig. 4. Snapshots for the evolution of the physical density.

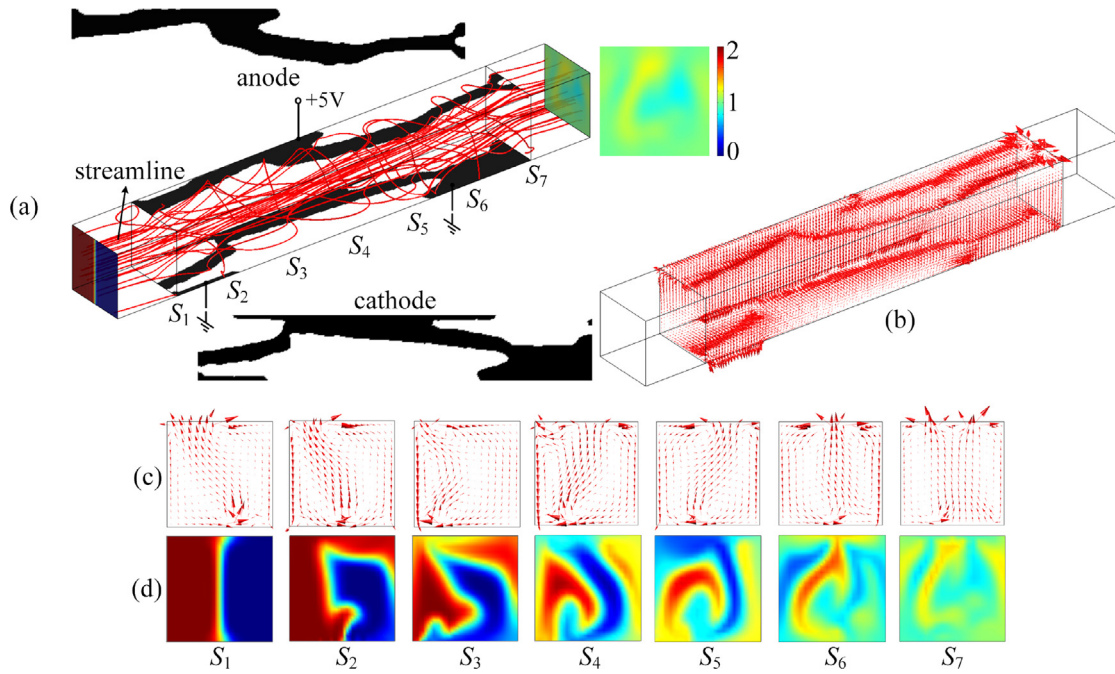


Fig. 6. (a) The derived electrode patterns and streamlines in the electroosmotic micromixer with electrical potential 5 V; (b) tangential velocity induced by the electrodes with the derived patterns at the walls of the micromixer; (c) distribution of the projected velocity vectors in the cross-sections of the electroosmotic micromixer; (d) concentration distribution in the cross-sections of the electroosmotic micromixer.

greatly enhance mixing through chaotic advection and strongly deform the interface between the impurities; equivalently, the diffusion area grows exponentially, and this make the mixing performance becomes efficient.

The chaotic advection in the electroosmotic microflow can be confirmed from the swirled and distorted streamlines in Fig. 6. For the steady flow, a streamline is the trajectory of a fluid-infinitesimal. As the fluid-infinitesimal moves along the corresponding distorted streamline, pressure and viscous force are imposed on it. The imposed pressure and viscous force can be equivalent to the composed action of a centrifugal, Coriolis, and Euler force, for which the centrifugal and Coriolis forces are perpendicular to the velocity of the fluid-infinitesimal, and the Euler force is parallel to the velocity of the fluid-infinitesimal (Fig. 7a). The density of the composed centrifugal and Coriolis force can be

computed from $\rho d\mathbf{u}/dt - \rho(d\mathbf{u}/dt \cdot \mathbf{u}/|\mathbf{u}|)\mathbf{u}/|\mathbf{u}|$, and the density of the Euler force from $\rho(d\mathbf{u}/dt \cdot \mathbf{u}/|\mathbf{u}|)\mathbf{u}/|\mathbf{u}|$, where t is the time and $d\mathbf{u}/dt$ is equal to $\mathbf{u} \cdot \nabla \mathbf{u}$ in the steady flow. The equivalent force density is plotted in Fig. 7b and c for the fluid-infinitesimals at different cross-sections. The chaotic distribution of the equivalent force density provides a dynamic mechanism for chaotic advection and swirled streamlines under the action of the electrode patterns. The mixing performance achieved by the electrodes is further confirmed by comparing the results to the case with the electrodes left unbiased (Fig. 8), where the mixing performance is improved more than 80-fold. After removing the electrodes, diffusion dominates the mixing performance, and the mixing efficiency decreases greatly because of the weak advection in the microflow with low Reynolds number; definitive improvement is achieved by chaotic advection with strongly swirled

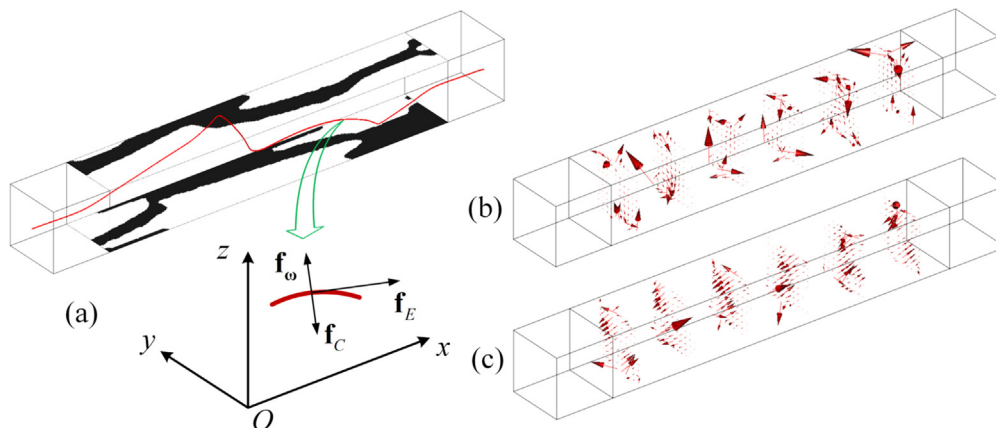


Fig. 7. (a) Sketch detailing the equivalent centrifugal force \mathbf{f}_ω , Coriolis force \mathbf{f}_c , and Euler force \mathbf{f}_E imposed on an infinitesimal volume of fluid; (b) composed centrifugal and Coriolis force density for the fluid-infinitesimals in different cross-sections; (c) Euler force density for the fluid infinitesimals at different cross-sections.

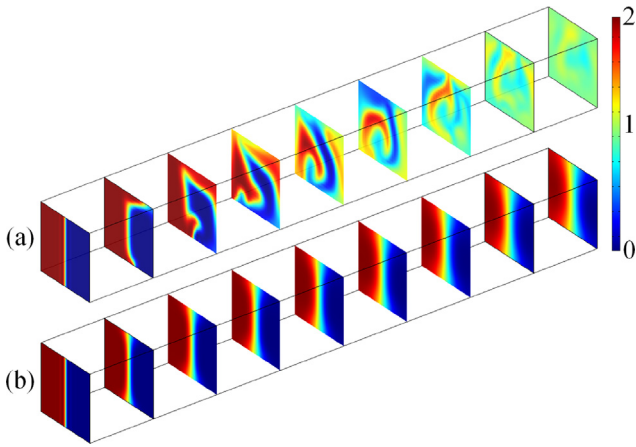


Fig. 8. Concentration distribution in the cross-sections of the electroosmotic micromixer, (a) with the inversely designed electrodes, and (b) with unbiased electrodes. The degree of mixing is improved by more than 80-fold as compared to the case with the electrodes left unbiased.

streamlines, when the electrodes with the derived patterns is localized on the walls.

Various parameters influence the outcome of the optimization procedure. These include the electric potential, mixing length, Péclet number and Reynolds numbers, feature size of the patterns, and the geometry of the microchannel. And the effects of these parameters are analysed as follows.

4.1. Effect of electric potential

The stronger the electrical potential, the higher the electrokinetic force acting within the channel, so that we expect that the optimized patterns of the electrodes will depend strongly on the applied voltage, and that the effective mixing length will increase as the voltage is lowered. In the numerical experiments, the geometry, mesh, and fluid properties are as before and shown in Fig. 2. The minimum feature size is controlled by setting $r = 2h_e$. Evaluation of the mixing performance Ψ versus different applied voltages is plotted in Fig. 9f, from which it is concluded that higher electrical potentials correspond to better mixing. This

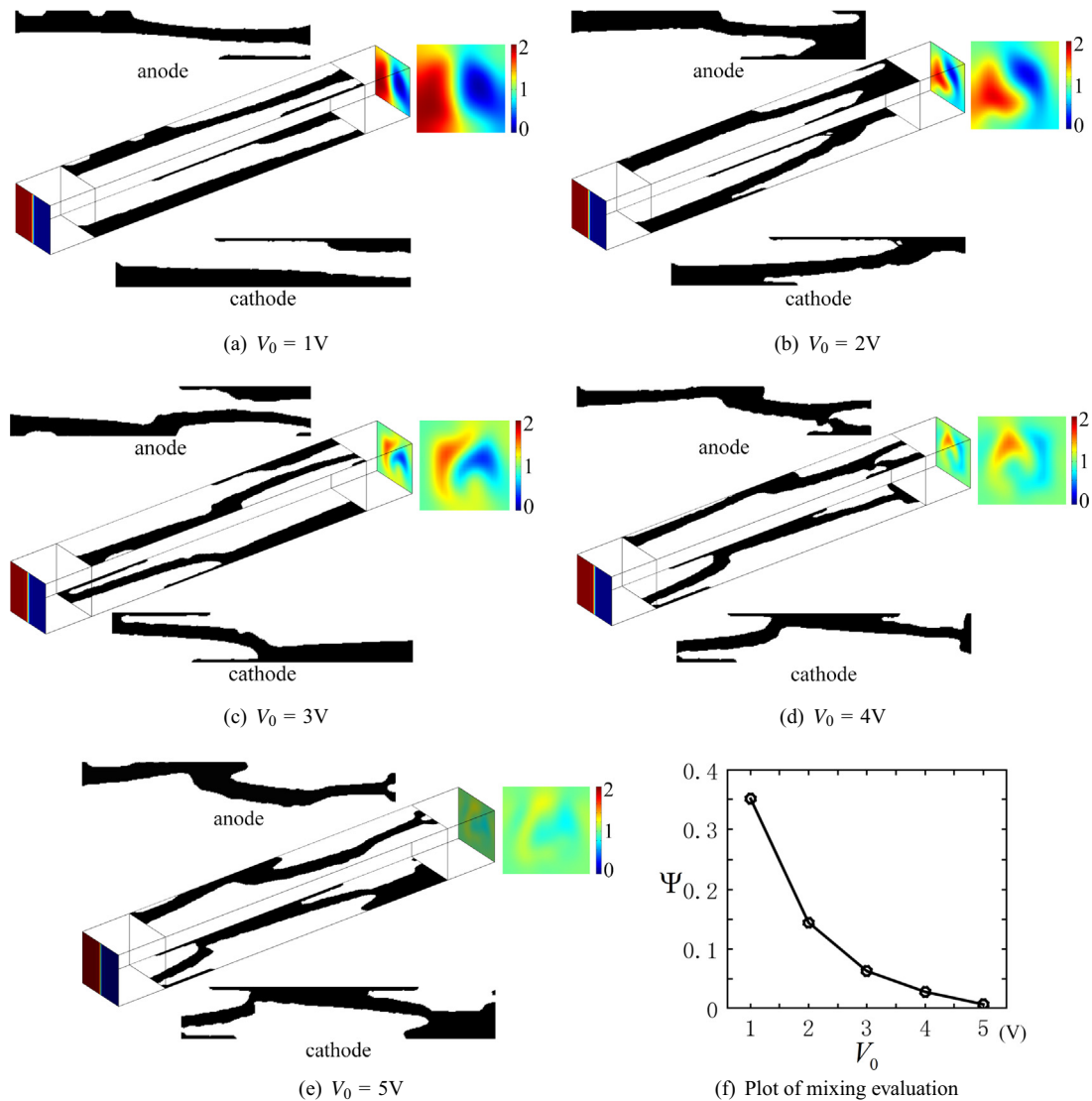


Fig. 9. (a)–(e) The derived electrode patterns corresponding to different applied electrical potentials; (f) plot of the mixing evaluations corresponding to the patterns in (a)–(e).

Table 2
Mixing evaluation Ψ calculated for every pair of electrode patterns in Fig. 9a–e, for different electric potentials.

	$V_0 = 1\text{ V}$	$V_0 = 2\text{ V}$	$V_0 = 3\text{ V}$	$V_0 = 4\text{ V}$	$V_0 = 5\text{ V}$
Fig. 9a	0.3518	0.1570	0.0824	0.0417	0.0121
Fig. 9b	0.3650	0.1435	0.0710	0.0420	0.0113
Fig. 9c	0.3821	0.1626	0.0623	0.0387	0.0097
Fig. 9d	0.3756	0.1711	0.0691	0.0280	0.0081
Fig. 9e	0.3597	0.1520	0.0728	0.0325	0.0072

is because these generate stronger electric fields, which induce more efficient disturbances and chaotic advection in the micro-flow. When the electrical potential was set to 4 V and 5 V (Fig. 9d and e), the achieved performance evaluation from perfect mixing was $\Psi = 0.0280$ and $\Psi = 0.0072$, considerably less than the threshold of $\Psi < 0.050$ defined in [99]. We surmise that the computed electrode patterns with the electrical potentials at 4 V and 5 V can achieve complete mixing over the length of the microchannel.

To confirm the optimality of the electrode patterns shown in Fig. 9a–e, the mixing evaluation Ψ is calculated for each pair of patterns for a range of applied voltages. The values in Table 2 confirms

that each electrode pair maximises its effect at its designated voltage, which is indicated in bold.

4.2. Effect of mixing length

To achieve different mixing lengths, the simulation model is varied by successively incrementing the fold number from 1 to 6, with all other parameters retained as defined for the original model. The computed electrode patterns are shown in Fig. 10a–f. The mixing is evaluated versus channel length, and plotted in Fig. 10g. Clearly and as expected, the degree of mixing improves with an increase in the mixing length.

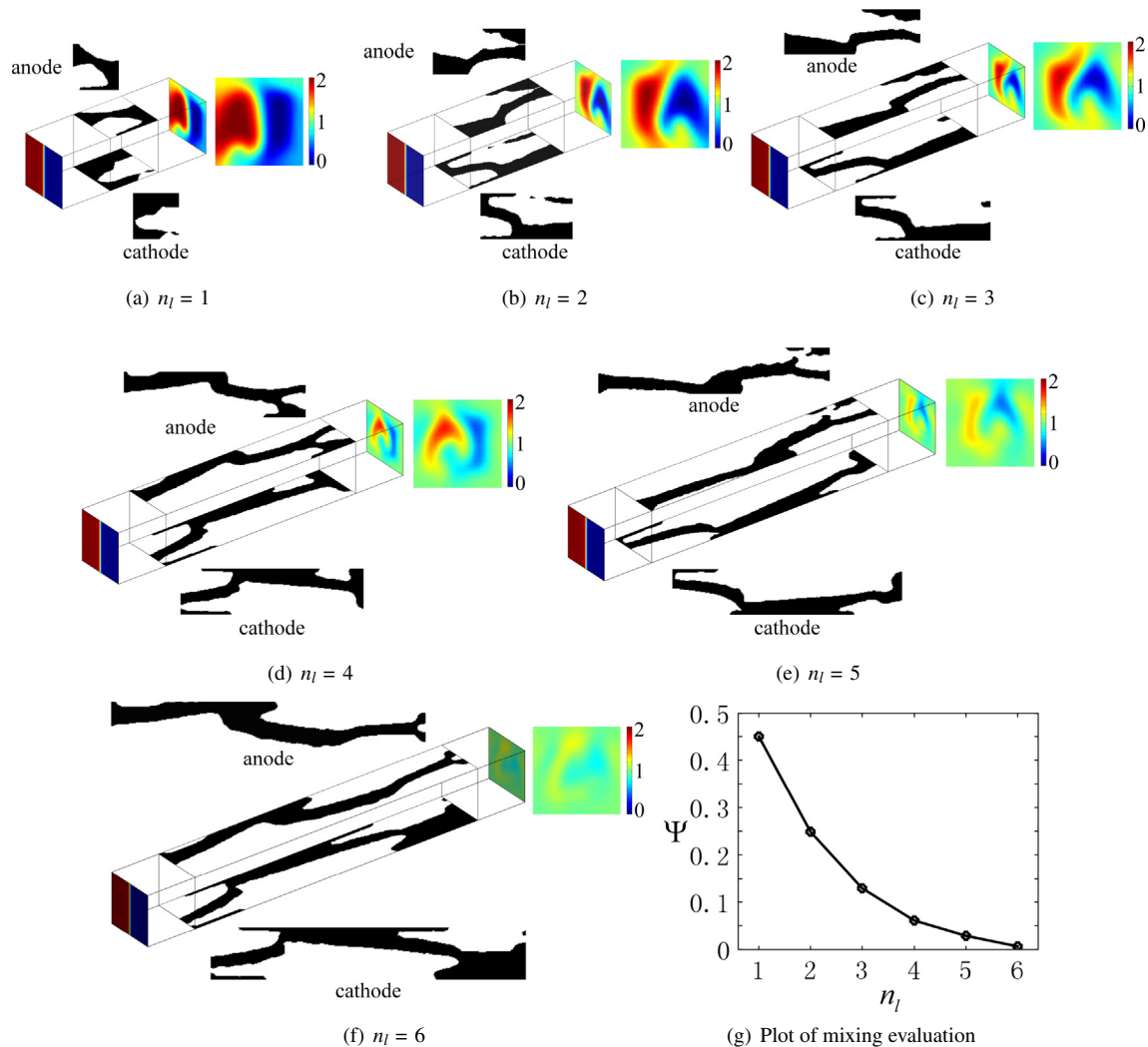


Fig. 10. (a)–(f) The derived electrode patterns for different mixing lengths; (g) plot of the mixing evaluations corresponding to the patterns in (a)–(e).

4.3. Effect of Péclet number and Reynolds number

We next investigate the effect of the Péclet number and Reynolds number on inversely designed electrode patterns. The Péclet number is used to measure the relative importance between convection (transferring the sample through the channel) and diffusion (interpenetration of the phases). For electrokinetic mixing, lower Péclet numbers should therefore be better, and this is confirmed by the results shown in Fig. 11, where the Reynolds number is held at $Re = 10$ and lower Péclet numbers correspond to better mixing performance.

The Reynolds number characterises the relative importance of convection versus the viscosity of the fluid. However, pipe Reynolds numbers below 2300 indicate laminar flow without turbulence, so that the Reynolds number mainly characterises the degree of convection. Because convection is an important parameter for micromixing, the value of the Reynolds number will influence the electrode patterns, with complete mixing favouring low Reynolds numbers, as confirmed by the results in Fig. 12, where the Péclet number is held at $Pe = 1 \times 10^3$. In the flows with low Reynolds numbers, the mixing progress is influenced predomi-

nantly by the diffusion, and the lateral convection of the flow can be strengthened by electroosmotic effect induced by the derived electrode patterns; the derived patterns corresponding to low Reynolds number have relatively better performance than those corresponding to relatively high Reynolds number, because higher Reynolds number represents higher longitudinal fluidic velocity, resulting in a short mixing time in the electroosmotic micromixer with fixed microchannel length, even though the electroosmotic micromixer has electrodes with reasonable patterns on its ceiling and floor walls.

4.4. Effect of feature size

Manufacturability is an important factor for electrode patterns, and depends mainly on the feature size of the derived electrode patterns and their multiplicity, which necessitates the use of a complex contacting layer. Both the feature size and multiplicity of the patterns can be controlled by the radius of the Helmholtz filter in Eq. (15). The effect of the feature size is investigated by setting the filter radius in a range of different values $r = nh_e, n \in \{1, 2, 3, 4, 5\}$, where h_e is the finite element size used

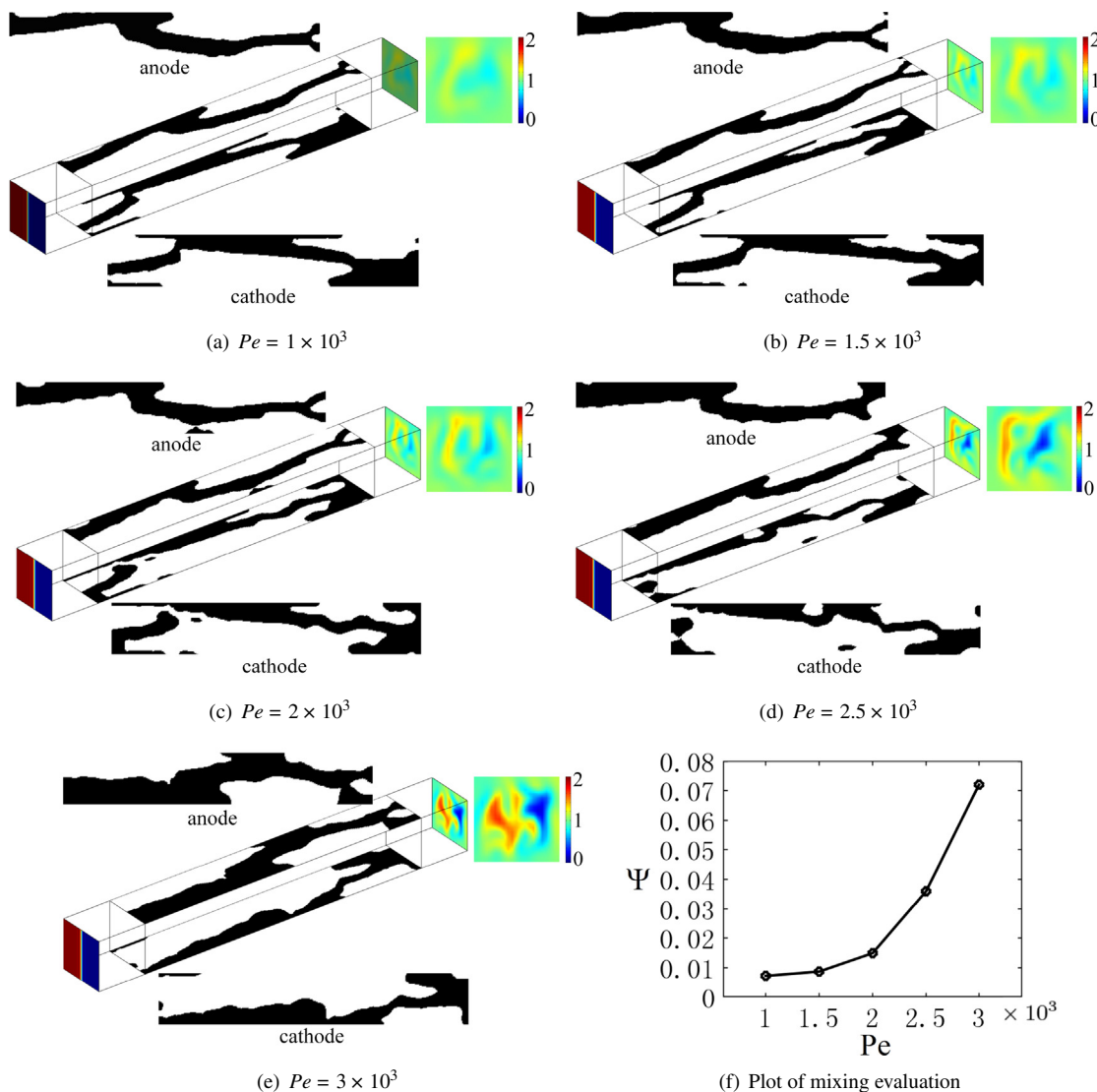


Fig. 11. (a)–(e) The derived electrode patterns of electroosmotic micromixers with different Péclet numbers; (f) plot of the mixing evaluations corresponding to the patterns in (a)–(e).

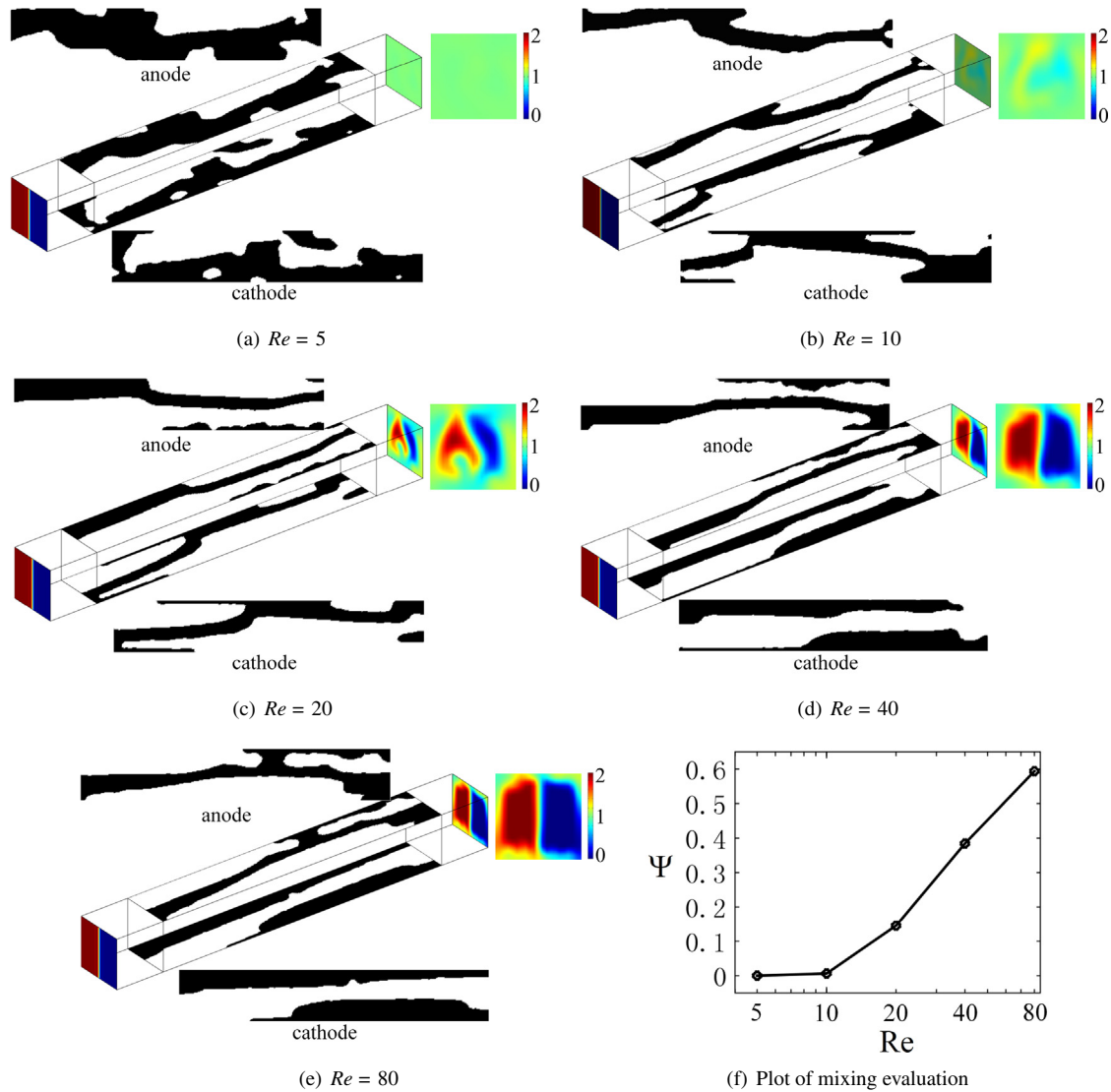


Fig. 12. (a)–(e) The derived electrode patterns of electroosmotic micromixers with different Reynolds numbers; (f) plot of the mixing evaluations corresponding to the patterns in (a)–(e).

to discretize the computational domain. Corresponding to these radii, the electrode patterns are computed as shown in Fig. 13a–e, and the corresponding degrees of mixing are plotted in Fig. 13f, where simplifications to the electrode patterns result in less effective mixing.

4.5. Effect of geometry

Curved microchannels are widely used to increase microfluidic integrability, extending mixing length and enhancing mixing performance by introducing the Dean effect [103]. Here we investigate the effect of combining curved channels with electrode patterns of electroosmotic micromixers. As sketched in Fig. 14, the central line of the microchannel forms an arc corresponding to different central angles, where the length of the arc is kept constant. Here \widehat{AB} is the central arc, R_c is the radius of the arc, and θ is the spanned angle. All other parameters are the same as those listed in Table 1.

When a fluid moves along a curved microchannel, there will be a transverse pressure gradient generated from the curvature, with an increase in pressure and a decrease in velocity close to the inner

wall, and the opposite effect at the outer side of the microchannel. This gives rise to a secondary flow in the cross-section of the microchannel, with the fluid in the center being swept towards the outer edge of the bend; the fluid near the wall returns towards the inside of the bend. This secondary flow induces the so-called Dean effect. The strength of the Dean effect is characterised by the Dean number, calculated to be $De = \rho U l / \eta \sqrt{l/2R_c} = Re \sqrt{l/2R_c}$ [103]. In microfluidics, the Dean number is proportional to the Reynolds number, and is inversely proportional to the square root of the radius $l/2R_c$. Microflows in micromixers usually have relatively low Dean numbers. The effect of the Dean number mainly corresponds to the effects of geometry for microflows with a fixed Reynolds number. In Fig. 14, different central angles of the central arc \widehat{AB} correspond to different Dean numbers. The electrode patterns are computed by varying the central angles for curved channels (Fig. 15a–e). The corresponding mixing evaluations are plotted in Fig. 15f. The results show that the electrodes remain fairly similar across the parameter variations, deformed along the bent channel, and that a stronger Dean effect with larger Dean number is helpful in enhancing the mixing efficiency.

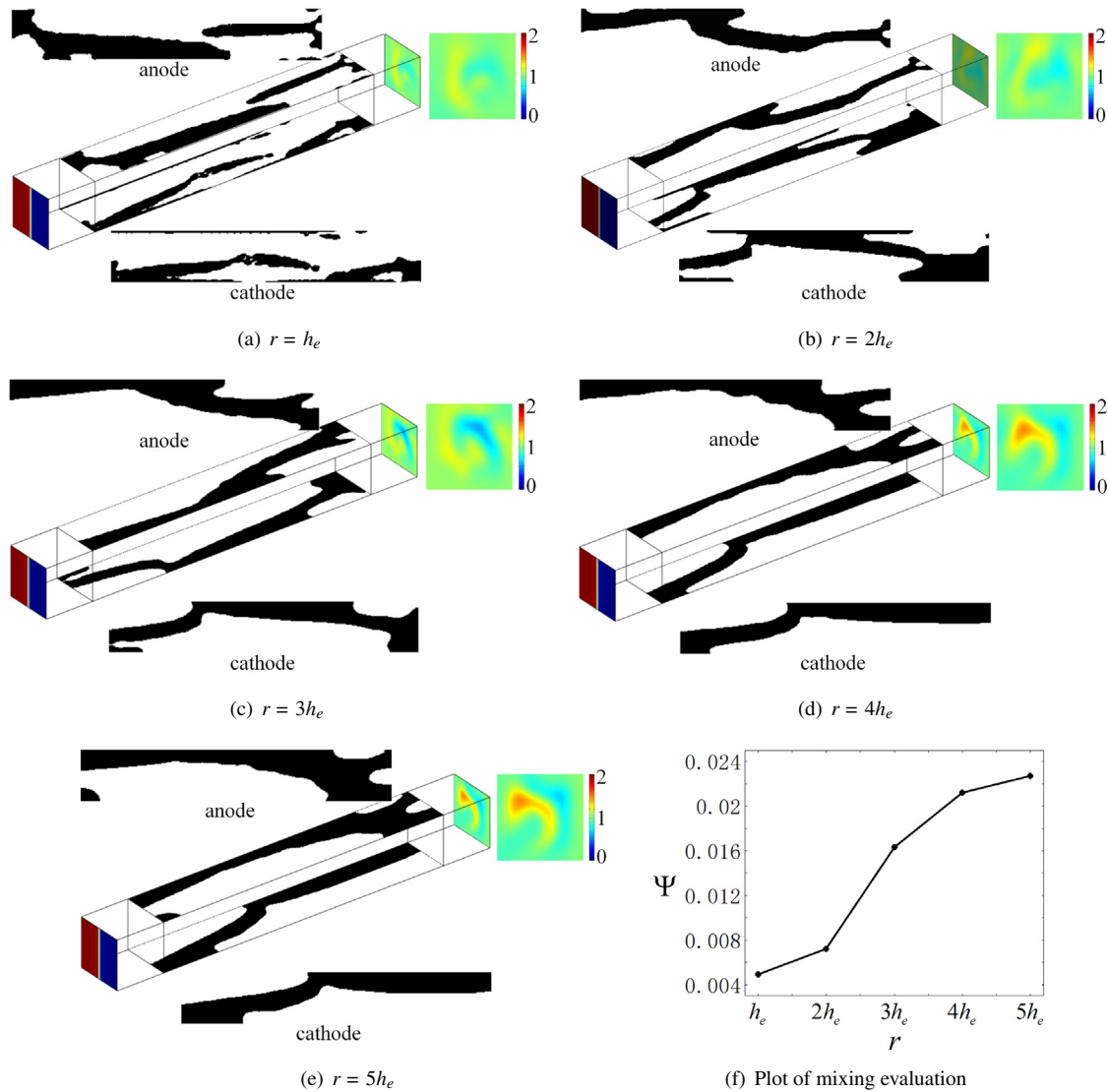


Fig. 13. (a)–(e) The derived electrode patterns of electroosmotic micromixers corresponding to different filter radii; (f) plot of the mixing evaluations corresponding to the patterns in (a)–(e).

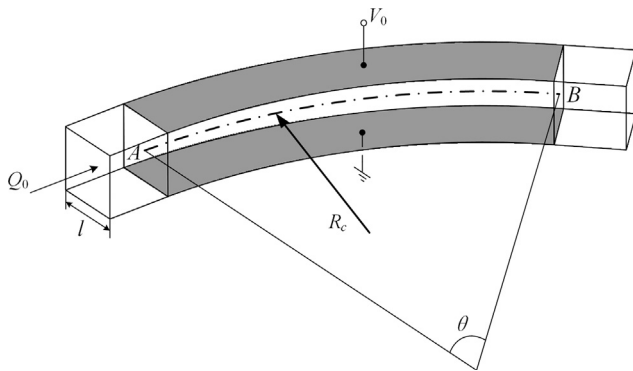


Fig. 14. Sketch for the computational domain of a curved electroosmotic-micromixer, where AB is the central arc, R_c is the radius of the arc and θ is the spanned angle.

5. Conclusion

This paper presented an inverse design method with which to determine the electrode designs for electroosmosis, a widely used

actuation mechanism in microfluidics. The method was implemented using the finite element method, embedded in a topology optimization approach. The electrode patterns for an electroosmotic micromixer were investigated with the goal to achieve the complete mixing of two fluids.

A variational problem was constructed, constrained by the Navier-Stokes equations and convection-diffusion equation defined in the microchannel, and a Helmholtz-Smoluchowski approximation at the walls, where the Helmholtz-Smoluchowski relation, derived based on the thin double layer approximation, is used to avoid modelling the Debye layer with much smaller feature size compared to that of the microfluidic channel. The variational problem was analyzed and solved using a Lagrangian multiplier-based adjoint method and a gradient information-based iterative procedure.

Several numerical results were computed to demonstrate the optimality of the inversely designed electrode patterns and the robustness of the method. The method can also be directly extended to provide a systematic approach for the electrode design of electroosmotic microfluidics, with potential applications in chemical reactors and biochemistry due to the outstanding performance of the derived electrodes. The research focused on DC

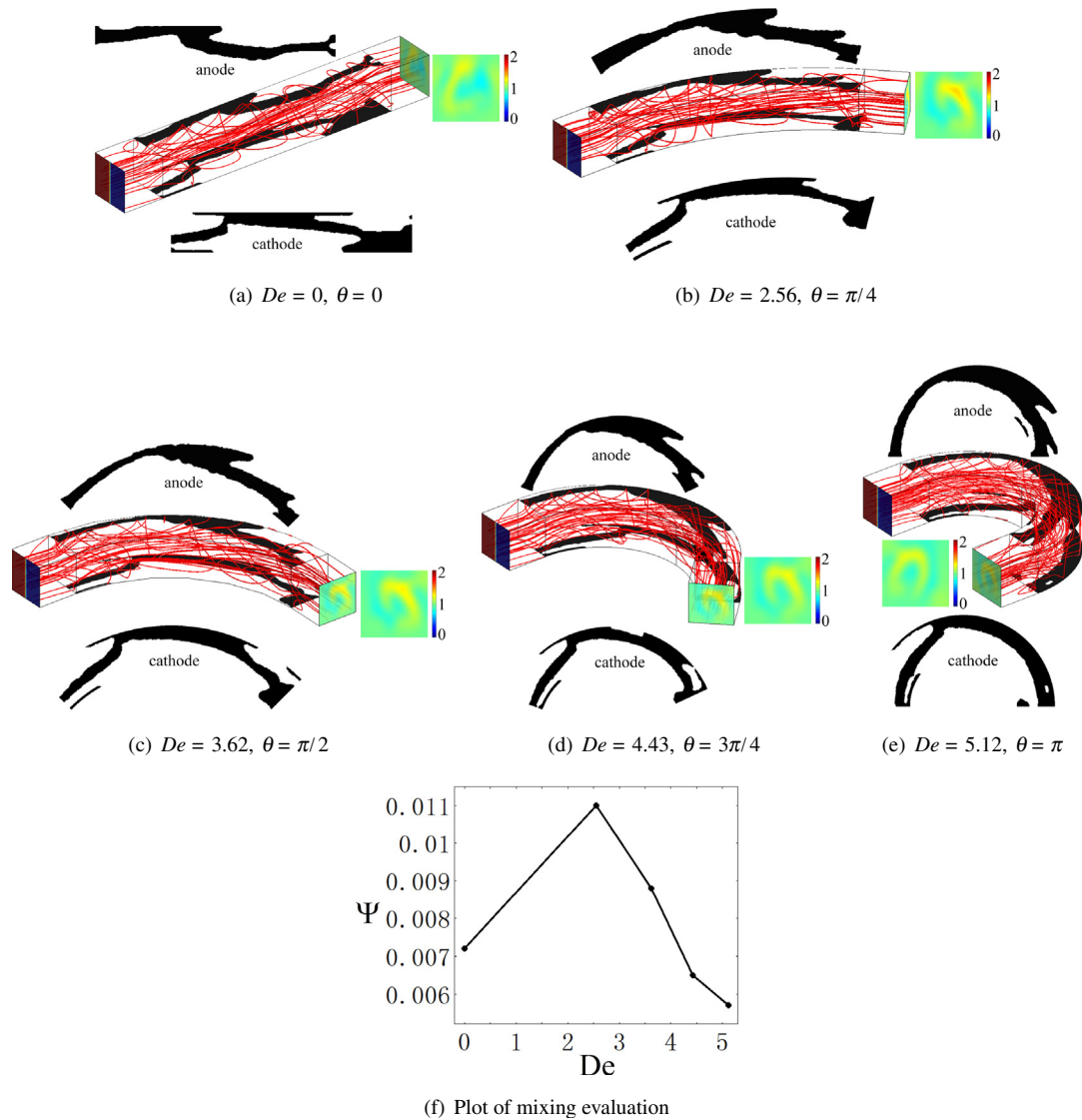


Fig. 15. (a)–(e) The derived electrode patterns of electroosmotic micromixers corresponding to different Dean numbers; (f) plot of the mixing evaluations corresponding to the patterns in (a)–(e).

(direct current) electroosmosis with steady microflows; it can also be used for AC (alternating current) electroosmosis with unsteady microflows, and can straightforwardly incorporate the Joule heating effect due to the electric field. These extensions will be investigated in our future work.

A novel feature of the implementation is the optimization over a lower-dimensional surface of an otherwise volumetric domain. Mathematically, the material interpolation is implemented between Dirichlet and Neumann types of boundary conditions. Therefore, it can be regarded to be a first step towards a class of topology optimization problems using surface structures to control bulk performance.

Conflict of interest

Authors declare that there is no conflict of interest.

Acknowledgements

This work was supported by the Humboldt Research Fellowship for Experienced Researchers (Humboldt-ID: 1197305), National Natural Science Foundation of China (No. 51405465, 61727813,

51605124), Youth Innovation Promotion Association of the Chinese Academy of Sciences (No. 2018253), and a Guest Professor Fellowship at the Karlsruhe Institute of Technology (KIT) via the DFG Metacoil project (KO 1883/20-1). During this project, J.G. Korvink was supported by an ERC Senior Grant (NMCEL, 290586), by the Karlsruhe School of Optics and Photonics (KSOP), and through the Cluster of Excellence BrainLinks-BrainTools (DFG, Grant No. EXC 1086). The authors are grateful to Prof. K. Svanberg for supplying the MMA codes; they are also grateful to the reviewers' kind attention and valuable suggestions.

Appendix A

To solve the partial differential equations in the constraints (PDEs) of the variational problem (Eq. (15)), a linear element-based finite element method is utilized for the weak forms of these PDEs [101]. The corresponding weak forms are:

- Find $V \in \mathcal{H}(\Omega)$ satisfying:

$$\int_{\Omega} \sigma \nabla V \cdot \nabla \hat{V} \, dv + \int_{\Gamma_{de}} \alpha V \hat{V} \, ds = 0, \quad \forall \hat{V} \in \mathcal{H}(\Omega); \quad (22)$$

- Find $\mathbf{u} \in (\mathcal{H}(\Omega))^3$, $p \in \mathcal{L}^2(\Omega)$, $\lambda_f \in (\mathcal{H}^{\frac{1}{2}}(\Gamma_w))^3$ and $\lambda_Q \in \mathbb{R}$ satisfying:

$$\begin{aligned} & \int_{\Omega} \rho(\mathbf{u} \cdot \nabla \mathbf{u}) \cdot \hat{\mathbf{u}} + [\eta(\nabla \mathbf{u} + \nabla \mathbf{u}^T) - p\mathbf{I}] : \nabla \hat{\mathbf{u}} - \hat{p} \nabla \cdot \mathbf{u} \, dv \\ & - \sum_{i=1}^{N_e} \int_{\Omega_i} \tau_{gls} \nabla p \cdot \nabla \hat{p} \, dv + \lambda_Q \int_{\Gamma_i} \hat{\mathbf{u}} \cdot \mathbf{n} \, ds + \hat{\lambda}_Q \left(\int_{\Gamma_i} \mathbf{u} \cdot \mathbf{n} \, ds - Q_0 \right) \\ & + \int_{\Gamma_w} \{ \mathbf{u} + \mu_{eo} [\nabla V - (\mathbf{n} \cdot \nabla V) \mathbf{n}] \} \cdot \hat{\lambda}_f + (\lambda_f - p\mathbf{n}) \cdot \hat{\mathbf{u}} \, ds = 0, \\ & \forall \hat{\mathbf{u}} \in (\mathcal{H}(\Omega))^3, \forall \hat{p} \in \mathcal{L}^2(\Omega), \forall \hat{\lambda}_f \in (\mathcal{H}^{\frac{1}{2}}(\Gamma_w))^3 \text{ and } \forall \hat{\lambda}_Q \in \mathbb{R}; \end{aligned} \tag{23}$$

- Find $c \in \mathcal{H}(\Omega)$ and $\lambda_c \in \mathcal{H}^{\frac{1}{2}}(\Gamma_i)$ satisfying:

$$\begin{aligned} & \int_{\Omega} \mathbf{u} \cdot \nabla c \hat{c} + D \nabla c \cdot \nabla \hat{c} \, dv + \sum_{i=1}^{N_e} \int_{\Omega_i} \tau_{supg} (\mathbf{u} \cdot \nabla c - D \nabla^2 c) (\mathbf{u} \cdot \nabla \hat{c}) \, dv \\ & + \int_{\Gamma_i} (c - c_i) \hat{\lambda}_c + \lambda_c \hat{c} \, ds = 0, \\ & \forall \hat{c} \in \mathcal{H}(\Omega) \text{ and } \forall \hat{\lambda}_c \in \mathcal{H}^{\frac{1}{2}}(\Gamma_i); \end{aligned} \tag{24}$$

- Find $\gamma_f \in \mathcal{H}(\Gamma_{de})$ satisfying:

$$\int_{\Gamma_{de}} r^2 \nabla_s \gamma_f \cdot \nabla_s \hat{\gamma}_f + \gamma_f \hat{\gamma}_f - \gamma \hat{\gamma}_f \, ds = 0, \quad \forall \hat{\gamma}_f \in \mathcal{H}(\Gamma_{de}), \tag{25}$$

where \hat{c} , $\hat{\mathbf{u}}$, \hat{p} , \hat{V} , $\hat{\gamma}_f$, $\hat{\lambda}_f$, $\hat{\lambda}_Q$ and $\hat{\lambda}_c$ are the test functions of the corresponding state variables, respectively; τ_{gls} and τ_{supg} are the stabilization parameters in Eq. (20).

Based on the weak forms of the PDE constraints, the augmented Lagrangian corresponding to the variational problem in Eq. (15) can be derived to be

$$\begin{aligned} \hat{\Psi} = & \frac{1}{\Psi_0} \int_{\Gamma_o} (c - \bar{c})^2 \, ds + \int_{\Omega} \sigma \nabla V \cdot \nabla V_a \, dv + \int_{\Gamma_{de}} \alpha V V_a \, ds \\ & + \int_{\Omega} \rho(\mathbf{u} \cdot \nabla \mathbf{u}) \cdot \mathbf{u}_a + [\eta(\nabla \mathbf{u} + \nabla \mathbf{u}^T) - p\mathbf{I}] : \nabla \mathbf{u}_a - p_a \nabla \cdot \mathbf{u} \, dv \\ & - \sum_{i=1}^{N_e} \int_{\Omega_i} \tau_{gls} \nabla p \cdot \nabla p_a \, dv + \lambda_Q \int_{\Gamma_i} \mathbf{u}_a \cdot \mathbf{n} \, ds + \lambda_{Qa} \left(\int_{\Gamma_i} \mathbf{u} \cdot \mathbf{n} \, ds - Q_0 \right) \\ & + \int_{\Gamma_w} \{ \mathbf{u} + \mu_{eo} [\nabla V - (\mathbf{n} \cdot \nabla V) \mathbf{n}] \} \cdot \lambda_{fa} + (\lambda_f - p\mathbf{n}) \cdot \mathbf{u}_a \, ds \\ & + \int_{\Omega} \mathbf{u} \cdot \nabla c c_a + D \nabla c \cdot \nabla c_a \, dv \\ & + \sum_{i=1}^{N_e} \int_{\Omega_i} \tau_{supg} (\mathbf{u} \cdot \nabla c - D \nabla^2 c) (\mathbf{u} \cdot \nabla c_a) \, dv \\ & + \int_{\Gamma_i} (c - c_i) \lambda_{ca} + \lambda_c c_a \, ds + \int_{\Gamma_{de}} r^2 \nabla_s \gamma_f \cdot \nabla_s \gamma_{fa} + \gamma_f \gamma_{fa} - \gamma \gamma_{fa} \, ds, \end{aligned} \tag{26}$$

where c_a , \mathbf{u}_a , p_a , V_a , and γ_{fa} are the adjoint variables of the corresponding state variables, respectively; λ_{fa} and λ_{Qa} are the adjoints of the Lagrangian multiplier λ_f and λ_Q , respectively; λ_{ca} is the adjoint of the Lagrangian multiplier λ_c . According to the Karush-Kuhn-Tucker conditions [100], the variational of $\hat{\Psi}$ should satisfy

$$\begin{aligned} \delta \hat{\Psi} = & \left\langle \frac{\partial \hat{\Psi}}{\partial V}, \delta V \right\rangle_{\mathcal{H}(\Omega)} + \left\langle \frac{\partial \hat{\Psi}}{\partial \mathbf{u}}, \delta \mathbf{u} \right\rangle_{(\mathcal{H}(\Omega))^3} + \left\langle \frac{\partial \hat{\Psi}}{\partial p}, \delta p \right\rangle_{\mathcal{L}^2(\Omega)} \\ & + \frac{\partial \hat{\Psi}}{\partial \lambda_Q} \delta \lambda_Q + \left\langle \frac{\partial \hat{\Psi}}{\partial c}, \delta c \right\rangle_{\mathcal{H}(\Omega)} + \left\langle \frac{\partial \hat{\Psi}}{\partial \lambda_c}, \delta \lambda_c \right\rangle_{\mathcal{H}^{\frac{1}{2}}(\Gamma_i)} \\ & + \left\langle \frac{\partial \hat{\Psi}}{\partial \gamma_f}, \delta \gamma_f \right\rangle_{\mathcal{H}(\Gamma_{de})} + \left\langle \frac{\partial \hat{\Psi}}{\partial \gamma}, \delta \gamma \right\rangle_{\mathcal{L}^2(\Gamma_{de})} = 0, \end{aligned} \tag{27}$$

at the optima of the variational problem in Eq. (15), where $\langle \cdot, \cdot \rangle$ is the operator used to implement the inner product on a corresponding functional space; δ is the operator used to implement the first order variational of a variable. Based on the adjoint method, the adjoint derivative of the variational problem in Eq. (15) can be computed to be

$$\delta \hat{\Psi} = \left\langle \frac{\partial \hat{\Psi}}{\partial \gamma}, \delta \gamma \right\rangle_{\mathcal{L}^2(\Gamma_{de})} \tag{28}$$

with the adjoint equations

$$\begin{aligned} & \left\langle \frac{\partial \hat{\Psi}}{\partial c}, \delta c \right\rangle_{\mathcal{H}(\Omega)} + \left\langle \frac{\partial \hat{\Psi}}{\partial \lambda_c}, \delta \lambda_c \right\rangle_{\mathcal{H}^{\frac{1}{2}}(\Gamma_i)} = 0; \\ & \left\langle \frac{\partial \hat{\Psi}}{\partial \mathbf{u}}, \delta \mathbf{u} \right\rangle_{(\mathcal{H}(\Omega))^3} + \left\langle \frac{\partial \hat{\Psi}}{\partial p}, \delta p \right\rangle_{\mathcal{L}^2(\Omega)} + \frac{\partial \hat{\Psi}}{\partial \lambda_Q} \delta \lambda_Q = 0; \\ & \left\langle \frac{\partial \hat{\Psi}}{\partial V}, \delta V \right\rangle_{\mathcal{H}(\Omega)} = 0; \\ & \left\langle \frac{\partial \hat{\Psi}}{\partial \gamma_f}, \delta \gamma_f \right\rangle_{\mathcal{H}(\Gamma_{de})} = 0; \end{aligned} \tag{29}$$

where

$$\begin{aligned} & \left\langle \frac{\partial \hat{\Psi}}{\partial c}, \delta c \right\rangle_{\mathcal{H}(\Omega)} + \left\langle \frac{\partial \hat{\Psi}}{\partial \lambda_c}, \delta \lambda_c \right\rangle_{\mathcal{H}^{\frac{1}{2}}(\Gamma_i)} \\ & = \int_{\Omega} \mathbf{u} \cdot \nabla \delta c c_a + D \nabla c_a \cdot \nabla \delta c \, dv \\ & + \sum_{i=1}^{N_e} \int_{\Omega_i} \tau_{supg} (\mathbf{u} \cdot \nabla c_a) (\mathbf{u} \cdot \nabla \delta c - D \nabla^2 \delta c) \, dv + \int_{\Gamma_i} \lambda_{ca} \delta c \\ & + c_a \delta \lambda_c \, ds + \frac{1}{\Psi_0} \int_{\Gamma_o} 2(c - \bar{c}) \delta c \, ds; \end{aligned} \tag{30}$$

$$\begin{aligned} & \left\langle \frac{\partial \hat{\Psi}}{\partial \mathbf{u}}, \delta \mathbf{u} \right\rangle_{(\mathcal{H}(\Omega))^3} + \left\langle \frac{\partial \hat{\Psi}}{\partial p}, \delta p \right\rangle_{\mathcal{L}^2(\Omega)} + \frac{\partial \hat{\Psi}}{\partial \lambda_Q} \delta \lambda_Q \\ & = \int_{\Omega} \rho [(\delta \mathbf{u} \cdot \nabla \mathbf{u}) \cdot \mathbf{u}_a + (\mathbf{u} \cdot \nabla \delta \mathbf{u}) \cdot \mathbf{u}_a] + \nabla \mathbf{u}_a \\ & : [\eta(\nabla \delta \mathbf{u} + \nabla \delta \mathbf{u}^T) - \delta p \mathbf{I}] - p_a \nabla \cdot \delta \mathbf{u} + \delta \mathbf{u} \cdot \nabla c c_a \, dv \\ & + \sum_{i=1}^{N_e} \int_{\Omega_i} -\tau_{gls} \nabla p_a \cdot \nabla \delta p \\ & + \left(\frac{\partial \tau_{supg}}{\partial \mathbf{u}} \cdot \delta \mathbf{u} \right) (\mathbf{u} \cdot \nabla c_a) (\mathbf{u} \cdot \nabla c - D \nabla^2 c) \\ & + \tau_{supg} (\delta \mathbf{u} \cdot \nabla c_a) (\mathbf{u} \cdot \nabla c - D \nabla^2 c) \\ & + \tau_{supg} (\mathbf{u} \cdot \nabla c_a) (\delta \mathbf{u} \cdot \nabla c) \, dv + \int_{\Gamma_i} \delta \lambda_Q \mathbf{u}_a \cdot \mathbf{n} + \lambda_{Qa} \delta \mathbf{u} \cdot \mathbf{n} \, ds \\ & + \int_{\Gamma_w} \lambda_{fa} \cdot \delta \mathbf{u} + (\delta \lambda_f - \delta p \mathbf{n}) \cdot \mathbf{u}_a \, ds; \end{aligned} \tag{31}$$

$$\left\langle \frac{\partial \Psi}{\partial V}, \delta V \right\rangle_{\mathcal{H}(\Omega)} = \int_{\Omega} \sigma \nabla V_a \cdot \nabla \delta V \, dV + \int_{\Gamma_{de}} \alpha V_a \delta V \, ds + \int_{\Gamma_w} \mu_{eo} [\nabla \delta V - (\mathbf{n} \cdot \nabla \delta V) \mathbf{n}] \cdot \boldsymbol{\lambda}_f \, ds; \quad (32)$$

$$\left\langle \frac{\partial \Psi}{\partial \gamma_f}, \delta \gamma_f \right\rangle_{\mathcal{H}(\Gamma_{de})} = \int_{\Gamma_{de}} r^2 \nabla_s \gamma_{fa} \cdot \nabla_s \delta \gamma_f + \gamma_{fa} \delta \gamma_f + (V - V_0) V_a \times \frac{\partial \alpha}{\partial \gamma_{fp}} \frac{\partial \gamma_{fp}}{\partial \gamma_f} \delta \gamma_f \, ds; \quad (33)$$

$$\left\langle \frac{\partial \Psi}{\partial \gamma}, \delta \gamma \right\rangle_{L^2(\Gamma_{de})} = \int_{\Gamma_{de}} -\gamma_{fa} \delta \gamma \, ds. \quad (34)$$

Then, based on the arbitrariness of the first order variational of the field variables in Eqs. (28) and (29), the weak forms of the adjoint equations in Eqs. (16)–(19) and the adjoint derivative in Eq. (21) can be derived.

References

- [1] R. Langer, Biomaterials: status, challenges and perspectives, *AIChE J.* 46 (2000) 1286–1289.
- [2] H.A. Stone, A.D. Strook, A. Ajdari, Engineering flows in small devices: microfluidics toward a lab-on-a-chip, *Annu. Rev. Fluid Mech.* 36 (2004).
- [3] A. Manz, N. Graber, H.M. Widmer, Miniaturized total chemical analysis systems: a novel concept for chemical sensing, *Sens. Actuators B* 1 (1990) 244.
- [4] S. Qian, H.H. Bau, A chaotic electroosmotic stirrer, *Anal. Chem.* 74 (2002) 3616–3625.
- [5] J.B. Zhang, G.W. He, F. Liu, electroosmotic flow and mixing in heterogeneous microchannels, *Phys. Rev. E* 73 (2006) 056305.
- [6] A. Brask, Principles of Electroosmotic Pumps (Master thesis), 2002. ISBN: 87-89935-31-4.
- [7] X. Wang, C. Cheng, S. Wang, S. Liu, Electroosmotic pumps and their applications in microfluidic systems, *Microfluid. Nanofluid.* 6 (2009) 145–162.
- [8] S. Zeng, C.H. Chen, J.C. Mikkelsen Jr., J.G. Santiago, Fabrication and characterization of electroosmotic micropumps, *Sens. Actuators B* 79 (2001) 107–114.
- [9] R.J. Hunter, Zeta Potential in Colloid Science: Principles and Applications, Academic, New York, 1981.
- [10] M. Ammam, Electrophoretic deposition under modulated electric fields: a review, *RSC Adv.* 2 (2012) 7633–7646.
- [11] E. Cummings, S. Griffiths, R. Nilson, P. Paul, Conditions for similitude between the fluid velocity and the electric field in electroosmotic flow, *Anal. Chem.* 72 (2000) 2526–2532.
- [12] I. Pagonabarraga, F. Capuani, D. Frenkel, Mesoscopic lattice modelling of electrokinetic phenomena, *Comput. Phys. Commun.* 169 (2005) 192–196.
- [13] T.J. Johnson, D. Ross, L.E. Locascio, Rapid microfluidic mixing, *Anal. Chem.* 74 (2002) 45–51.
- [14] C.C. Chang, R.J. Yang, Electrokinetic mixing in microfluidic systems, *Microfluid. Nanofluid.* 3 (2007) 501–525.
- [15] J. Smiatek, F. Schmid, Mesoscopic simulations of electroosmotic flow and electrophoresis in nanochannels, *Comput. Phys. Commun.* 182 (2011) 1941–1944.
- [16] F. Li, O. Ozen, N. Aubry, D.T. Papageorgiou, P.G. Petropoulos, Linear stability of a two-fluid interface for electrohydrodynamic mixing in a channel, *J. Fluid Mech.* 583 (2007) 347–377.
- [17] A. Kale, S. Patel, S. Qian, G. Hu, X. Xuan, Joule heating effects on reservoir-based dielectrophoresis, *Electrophoresis* 35 (2014) 721–727.
- [18] A. Sadeghi, M.H. Saidi, Z. Waezi, S. Chakraborty, Variational formulation on Joule heating in combined electroosmotic and pressure driven microflows, *Int. J. Heat Mass Trans.* 61 (2013) 254–265.
- [19] M. Jain, A. Yeung, K. Nandakumar, Induced charge electro osmotic mixer: obstacle shape optimization, *Biomicrofluidics* 3 (2009) 022413.
- [20] T.J. Johnson, L.E. Locascio, Characterization and optimization of slanted well designs for microfluidic mixing under electroosmotic flow, *Lab Chip* 2 (2002) 135–140.
- [21] H.S. Woo, B.J. Yoon, I.S. Kang, Optimization of zeta potential distributions for minimal dispersion in an electroosmotic microchannel, *Int. J. Heat Mass Trans.* 51 (2008) 4551–4562.
- [22] M.M. Gregersen, F. Okkels, M.Z. Bazant, H. Bruus, Topology and shape optimization of induced-charge electro-osmotic micropumps, *New J. Phys.* 11 (2009) 075019.
- [23] J. Wu, Ac electro-osmotic micropump by asymmetric electrode polarization, *J. Appl. Phys.* 103 (2008) 024907.
- [24] J.P. Urbanski, T. Thorsen, J.A. Levitan, M.Z. Bazant, Fast ac electro-osmotic micropumps with nonplanar electrodes, *Appl. Phys. Lett.* 89 (2006) 143508.
- [25] K. Matsubara, T. Narumi, Microfluidic mixing using unsteady electroosmotic vortices produced by a staggered array of electrodes, *Chem. Eng. J.* 288 (2016) 638–647.
- [26] J.H. Chen, Y.C. Lee, W.H. Hsieh, AC electroosmotic microconcentrator using a face-to-face, asymmetric electrode pair with expanded sections in the bottom electrode, *Microfluid. Nanofluid.* 20 (2016) 72.
- [27] A.K. Nayak, A. Haque, A. Banerjee, B. Weigand, Flow mixing and electric potential effect of binary fluids in micro/nano channels, *Colloids Surfaces A: Physicochem. Eng. Aspects* 512 (2017) 145–157.
- [28] C. Risco, R. López-Vizcaino, C. Sáez, A. Yustres, P. Cañizares, V. Navarro, M.A. Rodrigo, Remediation of soils polluted with 2,4-D by electrokinetic soil flushing with facing rows of electrodes: a case study in a pilot plant, *Chem. Eng. J.* 285 (2016) 128–136.
- [29] M.P. Bendsoe, O. Sigmund, *Topology Optimization-theory Methods and Applications*, Springer, Berlin, 2003.
- [30] A.G.M. Michell, The limit of economy of material in frame-structures, *Phil. Mag.* 8 (1904) 589–597.
- [31] M. Bendsoe, N. Kikuchi, Generating optimal topologies in optimal design using a homogenization method, *Comput. Methods Appl. Mech. Eng.* 71 (1988) 197–224.
- [32] O. Sigmund, A 99-line topology optimization code written in Matlab, *Struct. Multidisc. Optim.* 21 (2001) 120–127.
- [33] O. Sigmund, On the design of compliant mechanisms using topology optimization, *Mech. Struct. Mach.* 25 (1997) 495–526.
- [34] O. Sigmund, K.G. Hougaard, Geometric properties of optimal photonic crystals, *Phys. Rev. Lett.* 100 (2008) 153904.
- [35] J. Andkjær, O. Sigmund, Topology optimized low-contrast all-dielectric optical cloak, *Appl. Phys. Lett.* 98 (2011) 021112.
- [36] J. Andkjær, N.A. Mortensen, O. Sigmund, Towards all-dielectric, polarization-independent optical cloaks, *Appl. Phys. Lett.* 100 (2012) 101106.
- [37] G. Fujii, H. Watanabe, T. Yamada, T. Ueta, M. Mizuno, Level set based topology optimization for optical cloaks, *Appl. Phys. Lett.* 102 (2013) 251106.
- [38] A.R. Diaz, O. Sigmund, A topology optimization method for design of negative permeability metamaterials, *Struct. Multidisc. Optim.* 41 (2010) 163–177.
- [39] S. Zhou, W. Li, G. Sun, Q. Li, A level-set procedure for the design of electromagnetic metamaterials, *Opt. Express* 18 (2010) 6693–6702.
- [40] S. Zhou, W. Li, Y. Chen, G. Sun, Q. Li, Topology optimization for negative permeability metamaterials using level-set algorithm, *Acta Mater.* 59 (2011) 2624–2636.
- [41] J. Andkjær, S. Nishiwaki, T. Nomura, O. Sigmund, Topology optimization of grating couplers for the efficient excitation of surface plasmons, *JOSA B* 27 (2010) 1828–1832.
- [42] S. Zhou, W. Li, Q. Li, Level-set based topology optimization for electromagnetic dipole antenna design, *J. Comput. Phys.* 229 (2010) 6915–6930.
- [43] E. Hassan, E. Wadbro, M. Berggren, Topology optimization of metallic antennas, *IEEE Trans. Antennas Propag.* 62 (2014) 2488–2500.
- [44] Y. Deng, Z. Liu, C. Song, J. Wu, Y. Liu, Y. Wu, Topology optimization-based computational design methodology for surface plasmon polaritons, *Plasmonics* 10 (2015) 569–583.
- [45] Y. Deng, J.G. Korvink, Topology optimization for three-dimensional electromagnetic waves using an edge element-based finite-element method, *Proc. R. Soc. A* 472 (2016) 20150835.
- [46] H. Shim, V.T.T. Ho, S. Wang, D.A. Tortorelli, Level set-based topology optimization for electromagnetic systems, *IEEE Trans. Magn.* 45 (2009) 1582–1585.
- [47] T. Feichtner, O. Selig, M. Kiunke, B. Hecht, Evolutionary optimization of optical antennas, *Phys. Rev. Lett.* 109 (2012) 127701.
- [48] T. Nomura, K. Sato, K. Taguchi, T. Kashiwa, S. Nishiwaki, Structural topology optimization for the design of broadband dielectric resonator antennas using the finite difference time domain technique, *Int. J. Numer. Methods Eng.* 71 (2007) 1261–1296.
- [49] M.B. Dühring, J.S. Jensen, O. Sigmund, Acoustic design by topology optimization, *J. Sound Vib.* 317 (2008) 557–575.
- [50] G.I.N. Rozvany, Aims scope methods history and unified terminology of computer-aided optimization in structural mechanics, *Struct. Multidisc. Optim.* 21 (2001) 90–108.
- [51] M.P. Bendsoe, O. Sigmund, Material interpolations in topology optimization, *Arch. Appl. Mech.* 69 (1999) 635–654.
- [52] A. Gersborg-Hansen, M.P. Bendsoe, O. Sigmund, Topology optimization of heat conduction problems using the finite volume method, *Struct. Multidisc. Optim.* 31 (2006) 251–259.
- [53] W. Akl, A. El-Sabbagh, K. Al-Mitani, A. Baz, Topology optimization of a plate coupled with acoustic cavity, *Int. J. Solids Struct.* 46 (2008) 2060–2074.
- [54] S. Kreissl, G. Pingen, K. Maute, An explicit level-set approach for generalized shape optimization of fluids with the lattice Boltzmann method, *Int. J. Numer. Meth. Fluids* 65 (2011) 496–519.
- [55] S. Zhou, Q. Li, A variational level set method for the topology optimization of steady-state Navier-Stokes flow, *J. Comput. Phys.* 227 (2008) 10178–10195.
- [56] J.K. Guest, J.H. Prevost, Topology optimization of creeping fluid flows using a Darcy-Stokes finite element, *Int. J. Numer. Methods Eng.* 66 (2006) 461–484.
- [57] T. Borrvall, J. Petersson, Topology optimization of fluid in Stokes flow, *Int. J. Numer. Methods Fluids* 41 (2003) 77–107.
- [58] A. Takezawa, M. Haraguchi, T. Okamoto, M. Kitamura, Cross-sectional optimization of whispering-gallery mode sensor with high electric field

- intensity in the detection domain, *IEEE J. Sel. Top. Quant. Electron.* 20 (6) (2014) 1–10.
- [59] Y. Deng, Z. Liu, P. Zhang, Y. Liu, Y. Wu, Topology optimization of unsteady incompressible Navier–Stokes flows, *J. Comput. Phys.* 230 (2011) 6688–6708.
- [60] M.Y. Wang, X. Wang, D. Guo, A level set method for structural optimization, *Comput. Methods Appl. Mech. Eng.* 192 (2003) 227–246.
- [61] G. Allaire, F. Jouve, A. Toader, Structural optimization using sensitivity analysis and a level-set method, *J. Comput. Phys.* 194 (2004) 363–393.
- [62] Z. Liu, J.G. Korvink, Adaptive moving mesh level set method for structure optimization, *Eng. Optim.* 40 (2008) 529–558.
- [63] X. Xing, P. Wei, M.Y. Wang, A finite element-based level set method for structural optimization, *Int. J. Numer. Methods Eng.* 82 (2010) 805–842.
- [64] P.H. Guillaume, K.S. Idris, Topological sensitivity and shape optimization for the Stokes equations, *SIAM J. Cont. Optim.* 43 (2004) 1–31.
- [65] N. Aage, T.H. Poulsen, A. Gersborg-Hansen, O. Sigmund, Topology optimization of large scale stokes flow problems, *Struct. Multidisc. Optim.* 35 (2008) 175–180.
- [66] N. Wiker, A. Klarbring, T. Borrvall, Topology optimization of regions of Darcy and Stokes flow, *Int. J. Numer. Methods Eng.* 69 (2007) 1374–1404.
- [67] A. Gersborg-Hansen, O. Sigmund, R.B. Haber, Topology optimization of channel flow problems, *Struct. Multidisc. Optim.* 29 (2005) 1–12.
- [68] L.H. Olesen, F. Okkels, H. Bruus, A high-level programming-language implementation of topology optimization applied to steady-state Navier–Stokes flow, *Int. J. Numer. Methods Eng.* 65 (2006) 975–1001.
- [69] A. Evgrafov, Topology optimization of slightly compressible fluids, *ZAMM* 86 (2006) 46–62.
- [70] X. Duan, Y. Ma, R. Zhang, Shape-topology optimization for Navier–Stokes problem using variational level set method, *J. Comput. Appl. Math.* 222 (2008) 487–499.
- [71] G. Pinggen, K. Maute, Optimal design for non-Newtonian flows using a topology optimization approach, *Comput. Math. Appl.* 59 (2010) 2340–2350.
- [72] S. Nørgaard, O. Sigmund, B. Lazarov, Topology optimization of unsteady flow problems using the lattice Boltzmann method, *J. Comput. Phys.* 307 (2016) 291–307.
- [73] Y. Deng, Z. Liu, Y. Wu, Topology optimization of steady and unsteady incompressible Navier–Stokes flows driven by body forces, *Struct. Multidiscip. Optimiz.* 47 (2013) 555–570.
- [74] J.S. Romero, E.C.N. Silva, A topology optimization approach applied to laminar flow machine rotor design, *Comput. Methods Appl. Mech. Eng.* 279 (2014) 268–300.
- [75] Y. Deng, Z. Liu, Y. Wu, Topology optimization of capillary, two-phase flow problems, *Commun. Comput. Phys.* 22 (2017) 1413–1438.
- [76] F. Okkels, L.H. Olesen, H. Bruus, Application of topology optimization in the design of micro and nanofluidic systems, *NSTI-Nanotech.* (2005) 575–578.
- [77] F. Okkels, H. Bruus, Scaling behavior of optimally structured catalytic microfluidic reactors, *Phys. Rev. E* 75 (2007) 1–4.
- [78] C.S. Andreasen, A.R. Gersborg, O. Sigmund, Topology optimization of microfluidic mixers, *Int. J. Numer. Methods Fluids* 61 (2008) 498–513.
- [79] Y. Deng, Z. Liu, P. Zhang, Y. Wu, J.G. Korvink, Optimization of no-moving-part fluidic resistance microvalves with low Reynolds number, in: *IEEE MEMS Conference*, 2010, pp. 67–70.
- [80] Y. Deng, Z. Liu, P. Zhang, Y. Liu, Q. Gao, Y. Wu, A flexible layout design method for passive micromixers, *Biomed. Microdev.* 14 (2012) 929–945.
- [81] C.H. Villanueva, Kurt Maute, CutFEM topology optimization of 3D laminar incompressible flow problems, *Comput. Methods Appl. Mech. Eng.* 320 (2017) 444–473.
- [82] S. Osher, J.A. Sethian, Front propagating with curvature dependent speed: algorithms based on Hamilton–Jacobi formulations, *J. Comput. Phys.* 78 (1988) 12–49.
- [83] Y. Deng, Z. Liu, J. Wu, Y. Wu, Topology optimization of steady Navier–Stokes flow with body force, *Comput. Methods Appl. Mech. Eng.* 255 (2013) 306–321.
- [84] Y. Deng, P. Zhang, Y. Liu, Y. Wu, Z. Liu, Optimization of unsteady incompressible Navier–Stokes flows using variational level set method, *Int. J. Numer. Meth. Fluids* 71 (2013) 1475–1493.
- [85] O. Sigmund, K. Maute, Topology optimization approaches, *Struct. Multidiscip. Optim.* 48 (2013) 1031–1055.
- [86] N.T. Nguyen, Z. Wu, Micromixers—a review, *J. Micromech. Microeng.* 15 (2005) R1–R16.
- [87] W. Liu, Y. Ren, Y. Tao, B. Yao, Y. Li, Simulation analysis of rectifying microfluidic mixing with field-effect-tunable electrothermal induced flow, *Electrophoresis* (2017), <https://doi.org/10.1002/elps.201700234>.
- [88] N.A. Patankar, H.H. Hu, Numerical simulations of electroosmotic flow, *Anal. Chem.* 70 (1998) 1870–1881.
- [89] R.F. Probst, *Physicochemical Hydrodynamics: An Introduction*, Wiley, New York, NY, USA, 1994.
- [90] Y. Tao, W. Liu, Y. Ren, Y. Hu, G. Li, G. Ma, Q. Wu, On developing field-effect-tunable nanofluidic ion diodes with bipolar, induced-charge electrokinetics, *Micromachines* 9 (2018) 179.
- [91] W. Liu, Y. Ren, Y. Tao, B. Yao, N. Liu, Q. Wu, A universal design of field-effect-tunable microfluidic ion diode based on a gating cation-exchange nanoporous membrane, *Phys. Fluids* 29 (2017) 112001.
- [92] W. Liu, Y. Ren, Y. Tao, Y. Li, Q. Wu, On traveling-wave field-effect flow control for simultaneous induced-charge electroosmotic pumping and mixing in microfluidics: physical perspectives and theoretical analysis, *J. Micromech. Microeng.* 28 (5) (2018) 055004.
- [93] L. Formaggia, J.F. Gerbeau, F. Nobile, A. Quarteroni, Numerical treatment of defective boundary conditions for the Navier–Stokes equations, *SIAM J. Numer. Anal.* 40 (1) (2002) 376–401.
- [94] L. Formaggia, A. Veneziani, C. Vergara, A new approach to numerical solution of defective boundary value problems in incompressible fluid dynamics, *SIAM J. Numer. Anal.* 46 (6) (2008) 2769–2794.
- [95] B. Lazarov, O. Sigmund, Filters in topology optimization based on Helmholtz type differential equations, *Int. J. Numer. Methods Eng.* 86 (2011) 765–781.
- [96] J. Guest, J. Prevost, T. Belytschko, Achieving minimum length scale in topology optimization using nodal design variables and projection functions, *Int. J. Numer. Methods Eng.* 61 (2004) 238–254.
- [97] N.T. Nguyen, *Micromixer: Fundamentals, Design and Fabrication*, William Andrew, 2008.
- [98] S. Hossain, M.A. Ansari, K.Y. Kim, Evaluation of the mixing performance of three passive micromixers, *Chem. Eng. J.* 150 (2009) 492–501.
- [99] D. Li, *Encyclopedia of Microfluidics and Nanofluidics*, Springer, 2007.
- [100] M. Hinze, R. Pinnau, M. Ulbrich, S. Ulbrich, *Optimization with PDE Constraints*, Springer, 2009.
- [101] J. Donea, A. Hureta, *Finite Element Methods for Flow Problems*, Wiley, West Sussex, 2003.
- [102] K. Svanberg, The method of moving asymptotes: a new method for structural optimization, *Int. J. Numer. Meth. Eng.* 24 (1987) 359–373.
- [103] W.R. Dean, Note on the motion of fluid in a curved pipe, *Phil. Mag.* 20 (1927) 208–223.